Modeling of Time-of-arrival for CM4 Body Area Networks Channel

— effects of sensor location, human orientation and distance from access point

by

Yishuang Geng

A Thesis

Submitted to the Faculty

of the

WORCESTER POLYTECHNIC INSTITUTE

In partial fulfillment of the requirements for the

Degree of Master of Science

in

Electrical and Computer Engineering

by

May 2013

APPROVED:

Professor Kaveh Pahlavan, Major Thesis Advisor

Professor Yehia Massoud, Head of Department

Abstract

The rapid advancement in wireless technology, implantable medical devices and pervasive computing gave birth to a booming era of body area network (BAN) and BAN is finding an increasing number of applications in different fields. In-body networks enable innovative clinical treatments, on-body networks support real-time health monitoring and the networks between body surface and external access points connect the BAN to local area networks (LAN) and wide area networks (WAN), thus make the remote services come true.

The wireless channel between body surface and external access points is also the foundation of location-based service. With the awareness of location information becoming increasingly important for human beings, numerous potential localization applications for indoor human tracking and positioning have been identified. The requirement for high accuracy of human tracking on one hand challenges the system design and device manufacturing and on the other hand leads to in-depth investigation on the possible sources of ranging and localization error.

In Time-of-Arrival (TOA) based indoor human tracking system, the human body mounted with the target sensor can cause non-line-of-sight (NLOS) scenario and result in significant ranging error. In this thesis, we measured the TOA ranging error in a typical indoor environment and analyzed sources of inaccuracy in TOA-based indoor localization system. To quantitatively describe the TOA ranging error caused by human body, we introduce a statistical TOA ranging error model for body mounted sensors based on the measurement results. This model separates the ranging error into multipath error and NLOS error caused by the on-body creeping wave phenomenon. Both multipath error and NLOS error are modeled as a Gaussian

variable. The distribution of multipath error is only relative to the bandwidth of the system while the distribution of NLOS error is relative to the angle between human facing direction and the direction of Transmitter-Receiver, signal to noise ratio (SNR) and bandwidth of the system, which clearly shows the effects of human body on TOA ranging.

An efficient way to fight against the TOA ranging error caused by human body is to employ site-specific channel models by using ray-tracing technology. However, existing ray-tracing softwares lack the propagation model that takes the effects of human body into account. To address that issue, this thesis presents a empirical model for near human body ultra-wideband (UWB) propagation channel that is valid for the frequency range from 3GHz to 8GHz. It is based on measurements conducted in a anechoic chamber which can be regarded as free space. The empirical model shows the joint propagation characteristics of the on body channel and the channel between body surface and external access point. It includes the loss of the first path, arrival time of the first path and the total pathloss. Models for all three aspects have been partitioned into two sections by a break point due to the geometrical property of human body and the creeping wave phenomenon. The investigation on first path behavior can be regarded as a theoretical basis of ray-tracing technique that takes the effects of human body into consideration.

Acknowledgements

In this thesis I describe the research I conducted in pursuit of my Master of Science Degree in Electrical & Computer Engineering in Worcester Polytechnic Institute.

Firstly, I would like to offer my sincerest gratitude to my research advisor, Professor Kaveh Pahlavan, for leading me into the research field, for sharing his life experience and for providing financial support so that I could fully devote myself in to graduate study and research. Professor Pahlavan is a kindly mentor and a wise man. It is my greatest honor to have him as my advisor.

I am really grateful that I can have Professor Allen H. Levesque, Professor Thomas Eisenbarth and Professor Lifeng Lai as my committee members. Thank you for the valuable comments and reviewing of this thesis. I would like to thank Dr. Jie He from university of science and technology Beijing (USTB) for his help. Jie has offered me so many guide and suggestions as a co-advisor.

I also want to thank all the peers in lab CWINS, Guanqun Bao, Jin Chen, Zhuoran (Joanna) Liu, Ruijun Fu, Yadong Wan, Yunxing Ye, Pranay Swar, Shen Li and Umair Khan. Thank these people so much for offering me a nice atmosphere in the lab like a big family. I would like to delicate my thesis to my beloved parents, who offer me totally understanding, support and infinity love.

Contents

List of Figures

List of Tables

Chapter 1

Introduction

1.1 Background

Accurate indoor geolocation is an important and novel emerging technology for commercial, public safety, and military applications. It has many potential uses in different environments such as navigation in shopping centers, airports, hospitals, factories and museums as well as localization inside disaster areas and underground mines. Indoor geolocation is also instrumental in the growth of other areas of research, such as health monitoring, by associating the sensory information collected from body area networks with the geographical locations where the sensor data are collected [JHP12a] [JHe11a].

Since the satellite based Global Positioning System (GPS) does not provide satisfactory performance in indoor areas, new wireless technologies for indoor geolocation have been investigated since late-1990s. The received signal strength (RSS) base wireless localization techniques, currently used in smart devices, have their own limitations on accuracy, thus for more accurate localization researchers resort to TOA-based systems, used in GPS [NPe05]. The TOA-based systems, however,

suffer from the effects of intensive multipath conditions in indoor areas citeguv09. A number of algorithms have been proposed and implemented for the design of these systems for indoor geolocation and as a result, the accuracy of TOA-based localization is optimized to a great scale.

The wireless channel that indoor TOA-based localization system operates in is defined as the sub channel model 4 (CM4) in the standard documantation proposed by IEEE 802.15.6 [tg610]. The CM4 is referred to as the wireless channel from body surface external access points.

1.2 Motivation

With the advancement of technology, fairly acceptable localization results have been obtained when people try to track assets and properties [AP06a]. However, the performance of human tracking system suffers from a bottleneck of accuracy whenever the target sensors are located on the surface of human body [AMp03]. Such bottleneck comes from the fact that human body mounted with the target sensor can cause non-line of sight (NLOS) scenario and in such scenario wireless signal travels as creeping wave on the surface of human body. The creeping process is very complex. Previous studies on the behavior of indoor TOA ranging did not take the effects of human body into account and investigation in the effects of human body on TOA-based localization accuracy is in an urgent demand.

1.3 Contribution

The thesis consists of two major sections and the major contribution of this thesis has been listed as follows:

- Analysis on the effects human body orientation and sensor locations on TOA ranging error

  ·Chest mounted sensors

  ·Wrist mounted sensors

- An empirical ray tracing model for the effects of human body

  ·First path pathloss

  ·First path TOA

  ·Total pathloss

As is mentioned in the previous section, when investigating the effects of human body on TOA-based localization accuracy, the orientation and sensor locations have to be taken into consideration. Measurement of TOA ranging error has been conducted in a typical indoor environment with the target sensor mounted to the chest and wrist of human body. To quantitatively describe the TOA ranging error caused by human body, we introduce a statistical TOA ranging error model for body mounted sensors based on the measurement results. This model separates the ranging error into multipath error and NLOS error caused by the creeping wave phenomenon. Both multipath error and NLOS error are modeled as a Gaussian variable. The distribution of multipath error is only relative to the bandwidth of the system while the distribution of NLOS error is relative to the angle between human facing direction and the direction of Transmitter-Receiver, signal to noise ratio (SNR) and bandwidth of the system, which clearly shows the effects of human body on TOA ranging.

After the analysis on human body orientation and sensor location, a empirical model for near human body UWB propagation channel has been proposed with

respect to the distance between transmitter and receiver. The model is based on measurements conducted in a anechoic chamber which can be regarded as free space. The empirical model shows the joint propagation characteristics of the on body channel and the channel between body surface and external access point. It includes the loss of the first path, arrival time of the first path and the total pathloss. Models for all three aspects have been partitioned into two sections by a break point due to the geometrical property of human body and the creeping wave phenomenon. The investigation on first path behavior can be regarded as a theoretical basis of ray-tracing technique that takes the effects of human body into consideration.

1.4 Thesis Outline

The remainder of this thesis is organized as follow: Chapter 2 introduced the background of the researches mentioned in the thesis, such as the definition of body area networks, development status of the radio frequency localization technologies, wireless channel models used in indoor human tracking and the brief introduction of ray-tracing technique. Chapter 3 presented effects of human body on TOA ranging error with the target sensor mounted to human chest. Chapter 4 discussed the TOA ranging error of wrist mounted sensors. Chapter 5 proposed the UWB near body channel model. The near body model includes the pathloss of first path, time-of-arrival of the first path and the total pathloss. Last but not the least, Chapter 6 presented the conclusion of this thesis and discussion of the future work.

Chapter 2

Channel Modeling for BAN

2.1 Introduction

Recent advancements in electronics have enabled the development of small and intelligent medical sensors devices which can be worn on or implanted inside the human body. These sensors are able to send and receive as well as analyze and store the wirelessly transmitted data. Use of a wireless interface for such electronic devices is found to be efficient relative to wired connection which turns out to be cumbersome. Another advantage is that patient experiences a greater physical mobility and is no longer compelled to stay within a hospital. This whole process is considered to be the next step in mobile health innovation, enhancing personal health care and coping with the cost of current health care; this whole technology is called mobile heath or m-health, a step further from e-health which dealt with health care practice supported by electronic processes and communication. To fully exploit the benefits of m-heath a new area of specialization in wireless networks emerged, named Wireless Body Area Networks (WBANs).

Started as a Study Group in 2006 and motivated by the increasing research and

industry interest in WBANs, the IEEE Standards Association decided to form the IEEE 802.15 Task Group 6 in November 2007. A Body Area Network (BAN) or WBAN is formally defined by IEEE 802.15 as, "a communication standard optimized for low power devices and operation on, in or around the human body (but not limited to humans) to serve a variety of applications including medical, consumer electronics personal entertainment and other" [BLe11]. In more common terms, a Body Area Network is a system of devices in close proximity to a persons body that cooperate for the benefit of the user.

2.1.1 Frequency bands for BAN

For Body Area Network (BAN), there are several frequency bands which are always used for the related applications, for example, the MICS band(Medical Implant Communication Service) which is from 402MHz to 405MHz, the ISM band(Industrial, Scientific and Medical) , WMTS band (Wireless Medical Telemetry) and UWB band(Ultra Wide Band). All these bands are defined in the United States by Federal Communications Commission for the transmit data for patients health. Medical Implant Communication Service (MICS) is the frequency band between 401MHz and 406MHz, using for the communication with medical implant. It allows bi-directional radio communication with a pacemaker or other electronic implants. The maximum transmit power is very low, EIRP=25 microwatt, in order to reduce the risk of interfering with other users of the same band. The maximum used bandwidth at any one time is 300 kHz, which makes it a low bit rate system compared with Wi-Fi or Bluetooth. The main advantage is the additional flexibility compared to previously use inductive technologies, which required the external transceiver to touch the skin of the patient. MICS gives a range of a couple of meters [RR03]. The antenna in the Zarlink development kit is suitable for the MICS band [zar].

The industrial, scientific and medical (ISM) radio bands are reserved for the use of radio frequency (RF) energy for industrial, scientific and medical purposes other than communications. Examples of applications in these bands include radio-frequency process heating, microwave ovens, and medical diathermy machines. The powerful emissions of these devices can create electromagnetic interference and disrupt radio communication using the same frequency, so these devices were limited to certain bands of frequencies. In general, communications equipment operating in these bands must tolerate any interference generated by ISM equipment, and users have no regulatory protection from ISM device operation. Despite the intent of the original allocations, and because there are multiple allocations, in recent years the fastest-growing uses of these bands have been for short-range, low power communications systems. Cordless phones, Bluetooth devices, near field communication (NFC) devices, and wireless computer networks all use frequencies allocated to low power communications as well as ISM [Uni09]. There are many different frequency range, bandwidth and central frequency in the ISM band, and recently research for BAN using the ISM band are always in the 2.4MHz to 2.5MHz.

Wireless Medical Telemetry Service (WMTS) was created in 2000 because of interference issues due to establishment of digital television. The WMTS band has three different frequency bands, 608-614 MHz, 1395-1400 MHz and 1427-1432 MHz. Because of limitation of the devices, in addition to WMTS, many manufacturers have created devices that transmit data in the ISM bands such as 902-928 MHz, and, more typically, 2.4-2.5 GHz, often using IEEE 802.11 or Bluetooth radios.

Ultra-wide band (UWB) is a radio technology pioneered by Robert A. Scholtz and others which may be used at a very low energy level for short-range, high-bandwidth communications using a large portion of the radio spectrum [UWB founded wiki]. UWB is a technology for transmitting information spread over a

large bandwidth, lager than 500MHz. UWB has many applications including non-cooperative radar imaging, sensor data collection, precision locating and tracking applications. Ultra wideband was formerly known as "pulse radio", but the FCC and the International Telecommunication Union Radio communication Sector (ITU-R) currently define UWB in terms of a transmission from an antenna for which the emitted signal bandwidth exceeds the lesser of 500 MHz or 20% of the center frequency. Thus, pulse-based systemswhere each transmitted pulse occupies the UWB bandwidth (or an aggregate of at least 500 MHz of narrow-band carrier; for example, orthogonal frequency-division multiplexing (OFDM)can gain access to the UWB spectrum under the rules. Pulse repetition rates may be either low or very high. Pulse-based UWB radars and imaging systems tend to use low repetition rates (typically in the range of 1 to 100 megapulses per second). On the other hand, communications systems favor high repetition rates (typically in the range of one to two gigapulses per second), thus enabling short-range gigabit-per-second communications systems. Each pulse in a pulse-based UWB system occupies the entire UWB bandwidth (thus reaping the benefits of relative immunity to multipath fading, but not intersymbol interference), unlike carrier-based systems which are subject to deep fading and intersymbol interference.

2.1.2 Wireless Channel Model for Body Area Network

The ultimate limits on the performance of any communication system if the physical channel it operates in. When it comes to the BAN, the propagation characteristics of the wireless signal is becoming increasingly complex due the the influence of human body. In the standard document, a list of scenarios can be identified in which IEEE 802.15.6 devices will be operating. These scenarios along with their description and frequency band are listed in Table 2.1.2. The scenarios are determined based on

the location of the communicating nodes (i.e. implant, body surface and external). The scenarios are grouped into classes that can be represented by the same Channel Models (CM). These Channel Models has been also shown in Figure 2.1.

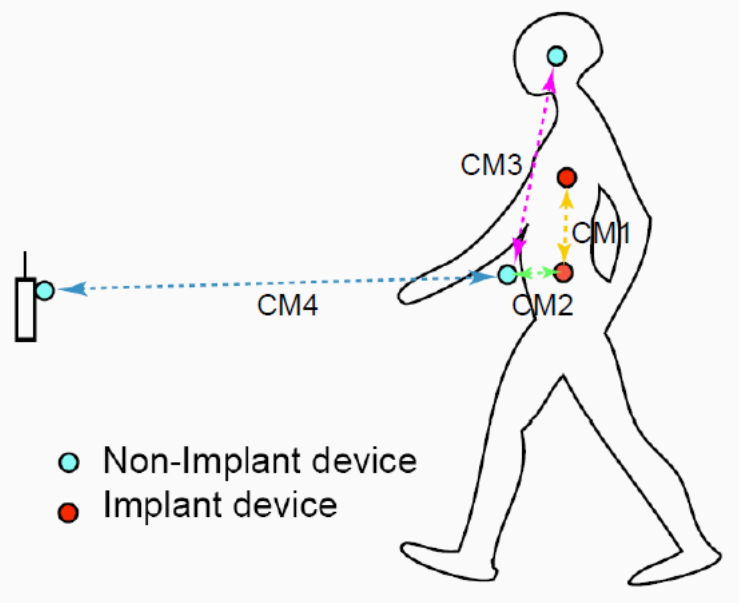

Figure 2.1: Possible communication links for Body Area Networking.

Fading

In the body area network communications, propagation paths can experience fading due to different reasons, such as energy absorption, reflection, diffraction, shadowing by body, and body posture. The other possible reason for fading is multipath due to the environment around the body. Fading can be categorized into two categories; small scale and large scale fading. Small scale fading refers to the rapid changes of the amplitude and phase of the received signal within a small local area due to small changes in location of the on-body device or body positions, in a given short period of time. The small scale fading can be further divided into flat fading and frequency selective fading. Large scale fading refers to the fading due to motion over

Table 2.1: List of scenarios and descriptions for BAN subchannels.

Scenario	Description	Frequency Band	Channel Model
S1	Implant to Implant	402-405 MHz	CM1
S2	Implant to Body Surface	402-405 MHz	CM2
S3	Implant to External	402-405 MHz	CM2
S4	Body Surface to Body Surface (LOS)	13.5, 50, 400, 600, 900 MHz 2.4, 3.1-10.6 GHZ	CM3
S5	Body Surface to Body Surface (NLOS)	13.5, 50, 400, 600, 900 MHz 2.4, 3.1-10.6 GHZ	CM3
S6	Body Surface to External (LOS)	900 MHz 2.4, 3.1-10.6 GHZ	CM4
S7	Body Surface to External (NLOS)	900 MHz 2.4, 3.1-10.6 GHZ	CM4

large areas; this is referring to the distance between antenna positions on the body and external node (home, office, or hospital).

Pathloss

Unlike traditional wireless communications, the path loss for body area network system (on body applications), is both distance and frequency dependent. The path loss model in dB between the transmitting and the receiving antennas as a function of the distance d based on the Friis formula in free space is described by **??**:

$$PL(d) = PL_0 + 10nlog_{10}(\frac{d}{d_0}) \tag{2.1}$$

where PL_0 is the path loss at a reference distance d_0, and n is the path-loss exponent. The path loss near the antenna depends on the separation between the antenna and the body due to antenna mismatch. This mismatch indicates that a body-aware antenna design could improve system performance.

Shadowing

Due to the variation in the environment surrounding of body or even movement of the body parts, path loss will be different from the mean value for a given distance as shown in equation (2.1). This phenomenon is called shadowing, and it reflects the path loss variation around the mean. The shadowing should be considered for stationary and non-stationary position of body. When considering shadowing, the total path loss PL can be expressed by:

$$PL = PL(d) + S \tag{2.2}$$

where $PL(d)$ is expressed by the equation (2.1) and S represents the shadowing component.

Power delay profile

Because of multipath reflections, the channel response of a BAN channel looks likes a series of pulses. In practice the number of pulses that can be distinguished is very large, and depends on the time resolution of the measurement system. The power delay profile of the channel is an average power of the signal as a function of the delay with respect to the first arrival path.

2.2 Radio Frequency Localization

For a TOA-based geolocation system, the time of flight of the direct path between a transmitter and a receiver is used to determine the intervening distance. A pulse is transmitted and the difference between the time of occurrence of the peak of the transmitted pulse and the first peak of the received pulse is used to measure the

TOA [PL05]. Reflections and blockage in indoor environment caused by walls, furniture and people moving inside the building result in rapid fluctuations of the power of the direct path and severe multipath conditions. In a multipath environment, the received waveform is combination of the pulse arriving on the direct path and pulses arriving on other paths between the transmitter and receiver. As a result, the shape of the transmitted waveform and the expected time of occurrence of the first peak of the received waveform are not preserved at the receiver and consequently the measured TOA of the direct path suffers from inaccuracies [Cra98]. The direct path can be blocked by large metallic objects [FAeA11] and large concrete walls or its first peak used for time of flight measurements may shift due to multipath components arriving close to the direct path [KPM02]. These errors in the TOA estimation cause ranging errors that are a function of the environment and bandwidth of the measurement system [AP06b]. For realistic performance evaluation of TOA-based indoor geolocation systems, it is traditional to classify different multipath conditions and physical situations causing these conditions [NAP09].

2.2.1 Multipath Conditons and Ranging Error

In a multipath rich indoor area, the overall channel impulse response between a transmitter and a receiver, $h(t, \tau)$, is given by:

$$h(t, \tau) = \sum_{i=1}^{N} \beta_i e^{j\phi} \delta(t - \tau_i) \tag{2.3}$$

where β_i and ϕ_i represent the amplitude and phase of the i^{th} path arriving at delay τ_i [PL05]. The parameter N is the number of paths between the transmitter and the receiver. If the transmitted waveform is represented by $x(t)$ the received waveform, $y(t)$, is given by

This received signal is often referred to as the channel profile. In indoor geolocation the Hamming pulses are commonly used as the transmitted waveform. The Hanning pulses have very low side lobes allowing detection of more multipath components and they are defined as:

$$\omega(n) = \begin{cases} 0.54 - 0.46\cos(\frac{2\pi n}{N}), & 0 \leq n \leq N \\ 0, & \text{otherwise} \end{cases} \tag{2.4}$$

where T is length window.

Figure 2.2 shows two typical measured channel profiles in an office environment. If we normalize the peak of the transmitted pulse at time zero, the peak of the first arriving pulse is the measurement of the TOA. The estimated distance between the transmitter and the receiver is $\hat{d} = \tau_l \times c$, in which c is the speed of radio wave propagation in the medium. In free space it is the same as speed of light and in other media such as inside the human body it will vary with the conductivity of the medium [KK09].

For TOA-based indoor geolocation, multipath conditions can be classified into two categories based on the availability of direct path (DP) between the transmitter and the receiver [Cra98]. The first category is detectable direct path (DDP), in which the amplitude of the direct path pulse is higher than the threshold of the receiver and is detectable, as shown in figure 2.2 (a). The second category is undetectable direct path (UDP), shown in figure 2.2 (b), in which the power of the direct path pulse is lower than the threshold of the receiver and thus the direct path pulse is undetectable. If the amplitude of the direct path in the received multipath profile

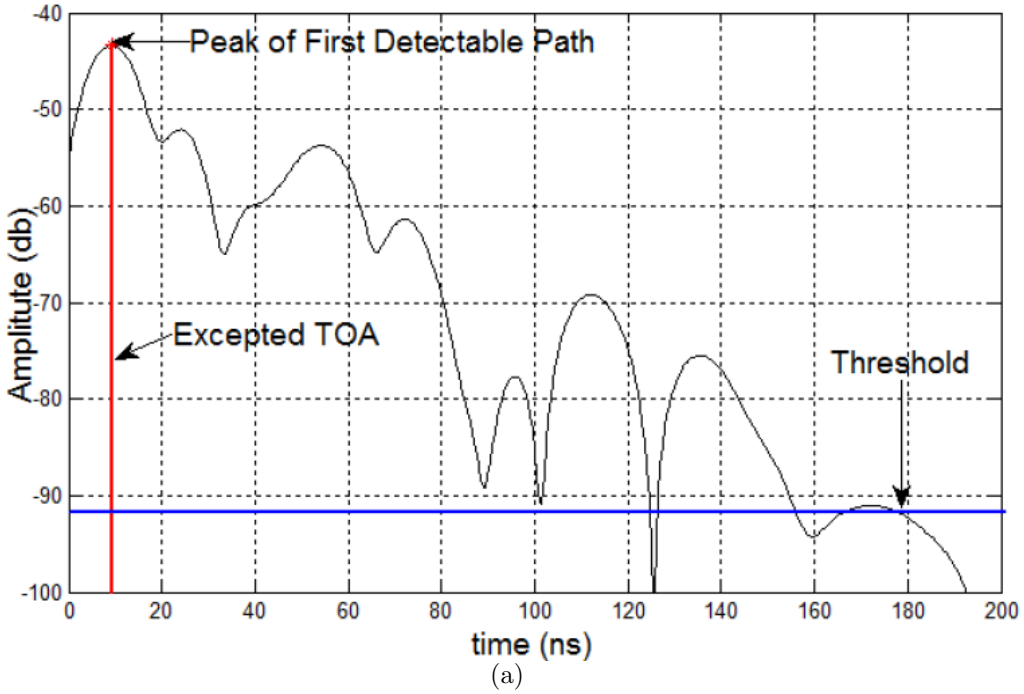

(a)

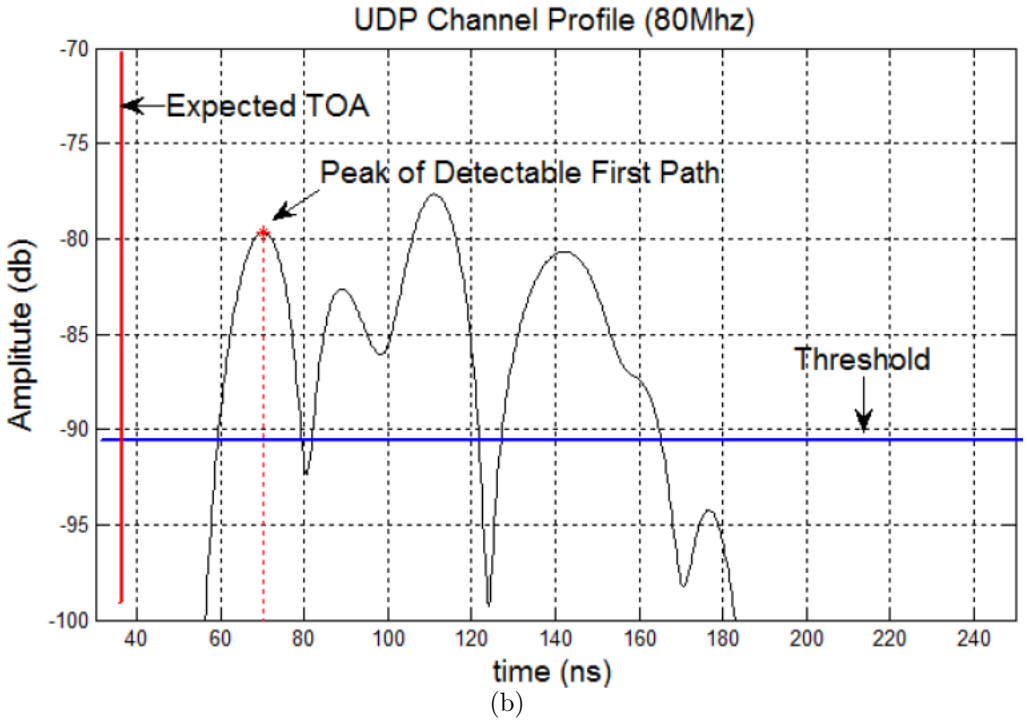

(b)

Figure 2.2: DDP and UDP conditions in atypical indoor area.

is represented by β_{DP}, the DDP and UDP are defined as:

$$y(t) = \begin{cases} DDP, & \beta_{DP} \geq \beta_T \\ UDP, & \beta_{DP} < \beta_T \end{cases} \tag{2.5}$$

where β_T is the power threshold of the receiver.

In DDP condition, shown in figure 2.2 (a), we have a small difference between the expected TOA and the measured value of the TOA. This difference is caused by the shift of the peak of the received waveform from the expected location after the signal arriving from other paths is added to the signal from the direct path. The shift in the location of the peak is mostly caused by the paths arriving close to the direct path arrival time. In UDP condition, shown in figure 2.2 (b), the direct path is blocked by objects situated between the transmitter and the receiver and it cannot be detected at all. In TOA-based ranging, this condition causes significantly large ranging errors .

2.2.2 Physical Scenarios for Multipath Condition

The physical environment around and between the transmitter and receiver determines the multipath condition. These multipath conditions affect the performance of TOAbased geolocation systems. The multipath conditions for indoor geolocation can be classified into four different physical scenarios: free space, line of sight (LOS), nonLOS-DDP (NLOS-DDP) and NLOS-UDP.

In free space, the receiver can easily detect the direct path and ranging accuracy is determined by the implementation of the device, including accuracy of the synchronization scheme, accuracy of the signal detection scheme, frequency of the timer used to record the transmit time and arrival time of the pulse.

In the LOS scenario for an indoor area there is no obstruction between the transmitter and the receiver and the direct path is always the strongest path. However, paths arriving in close vicinity of the direct path will shift the peak of the first path causing modest ranging errors [AP06b]. The ranging accuracy is affected by the bandwidth of the pulse and the strength of the multipath components close to the

direct path as well as the device implementation details. The ranging error in LOS scenarios is expected to be larger than ranging error in free space scenario.

In the NLOS-DDP scenario, the direct path between the transmitter and the receiver is obstructed by objects with low attenuation coefficients, such as wooden walls, rock walls and furniture. In this scenario, usually, the direct path pulse is weakened, but still available in the received signal. This situation makes it more difficult to detect the TOA of the direct path pulse and to estimate the distance between the transmitter and the receiver. The ranging error in this scenario is expected to be larger than ranging error in the LOS scenario.

In the NLOS-UDP scenario, the direct path between the transmitter and the receiver is obstructed by objects with high attenuation coefficients that submerge the direct path pulse below the detection threshold. These situations are observed when large metallic objects such as elevators or concrete walls are situated between the transmitter and the receiver. In this scenario, the ranging error is expected to be much larger than the ranging error in the other scenarios.

2.3 Ray-Tracing Technology

In indoor environments, performance of TOA-based ranging and localization algorithms and systems is significantly influenced by the extensive multipath conditions in the channel between a device to be localized and the Reference Nodes or fixed Reference Points in known locations that are used to locate the device. Since each deployment of infrastructure for the Reference Points has a specific architecture resulting in a specific multipath condition among Reference Points and the targeted device, the ranging and localization performance of TOA location systems can vary widely across different indoor environments. In such condition, site-specific models

will be much more accurate and reliable compared to the statistical models proposed in the standard documentation. Traditional statistical models proposed in the standard documentation suffer the lack of accuracy due to the fact that statistical models are derived from extensive measurement results which are not specific to the intended deployment environment. As a consequence, site-specific models attracts more and more attention for high accuracy localization applications. Ray-tracing is a useful tool to create site-specific channel models.

In nature, a light source emits a ray of light which travels, eventually, to a surface that interrupts its progress. One can think of this "ray" as a stream of photons traveling along the same path. In a perfect vacuum this ray will be a straight line (ignoring relativistic effects). Any combination of four things might happen with this light ray: absorption, reflection, refraction and fluorescence. A surface may absorb part of the light ray, resulting in a loss of intensity of the reflected and/or refracted light. It might also reflect all or part of the light ray, in one or more directions. If the surface has any transparent or translucent properties, it refracts a portion of the light beam into itself in a different direction while absorbing some (or all) of the spectrum (and possibly altering the color). From here, the reflected and/or refracted rays may strike other surfaces, where their absorptive, refractive, reflective and fluorescent properties again affect the progress of the incoming rays. Some of these rays travel in such a way that they hit our eye, causing us to see the scene and so contribute to the final rendered image.

As for wireless channel modeling, ray-tracing technique is an approach that can obtain channel characteristic by identifying the contributions of individual multipath component and calculating their composition at the receiver. Since each individual multipath component is described in terms of rays, optical effects such as absorption, reflection and diffraction of surrounding walls and stuff that make up the indoor

environment can be taken into account. As for BAN applications, human body itself also has a strong influence on the waveform propagation and it can be regarded as a special and complex obstacle to the passing rays. However, no ray-tracing model considering human body can be found in the open literature until now.

Chapter 3

Modeling the TOA Ranging Error for Chest Mounted Sensors

3.1 Introduction

Nowadays, the rapid development of ultra wide band (UWB) technology in the wireless industry not only provides high data rate wireless communication, but also realizes the precise TOA-based indoor localization. With the awareness of localization information becoming increasingly important for human beings, numerous potential localization applications for indoor human tracking and positioning have been identified. These applications are widely used for security and health purposes such as monitoring patients in the hospital, navigating firefighters in the burning house, locating miners in the underground environment and even tracking soldiers in the battle field [NMP06] [KP02]. The requirement of higher localization accuracy for indoor human tracking system on one hand challenges the system design and device manufacturing and on the other hand leads to in-depth investigation on the possible sources of TOA ranging error. In typical indoor localization system,

target sensors are often mounted to the surface of human body and the distances between target sensor and external base stations are measured to calculate the targets position [JHP12b].

Superior to the well-known received signal strength (RSS) based and angle-of-arrival (AOA) based indoor localization technologies, TOA-based localization is famous for its extraordinary accuracy and practical features [KP02] [JHW12] [ZB12]. In a typical indoor environment, with efficient algorithm and enough sampling, the median ranging error of RSS-based or AOA-based localization goes up to 3 meters [EAM11, CPe10]. However, given adequate system bandwidth, the median ranging error of TOA-based localization can be limited within 1.5 meters [JHW12]. For TOA-based localization, narrow impulse signals are transmitted from the target node to the reference nodes with known location. By measuring the impulse propagation time, distance between sensor node and base station can be easily estimated by multiplying the propagation time with the velocity of the signal.

3.1.1 Source of TOA Ranging Error

In indoor environment, the accuracy of TOA ranging is correlated to the multipath condition of the wireless channel, since only the propagation time of the impulse in direct path represents the actual distance. In a multipath rich environment, impulse always combines with the neighbor multipath components [JHW12]. The direct path is unable to be distinguished and the most efficient way to estimate the arrival time of received signal is to measure the arrival time of the first peak above threshold in receive signal profile. In Line-if-Sight (LOS) scenario, the ranging error comes from multipath error, which is caused by combination of the direct path and its neighboring multipath components [LS02]. In NLOS scenario, the NLOS error is caused by the blockage of direct path. Compare to the multipath error,

NLOS error contributes more to the localization inaccuracy due to the fact that the signal strength of direct path is so strongly attenuated that it often drops below the threshold and becomes undetectable [DDe09] [HP08]. When the direct path has been failed to be detected, the first adjacent path over the threshold will be considered as the direct path, leading to significant ranging and localization error.

The IEEE 802.15.6 standard defines the body surface sensor node as a node that is placed on the surface of human skin or at most 2 centimeters away [KPK12a]. In that situation, human body can be regarded as a smooth and bended surface on which the wireless signal can be diffracted and travels in the pattern of creeping wave [SPK12]. Consequently, apart from the NLOS error cause by the penetration loss of human body, the creeping wave around the surface of human body also contribute to the inaccuracy of TOA-based indoor localization. Due to the complexity of penetration and creeping process of wireless signal, it is very difficult and not necessary to solely identify the NLOS error and ranging error caused by creeping wave. However, knowing the joint effect of the involvement of human body is significantly helpful in evaluating the human tracking systems performance as well as designing localization algorithms.

When the target nodes are mounted to the surface of human body, the characteristics of the radio propagation channel between target node and reference node changes according to the involvement of the human body. In most of the indoor human tracking systems, the target nodes are mounted on the surface of human body and TOA ranging performs in both the channel from body surface to body surface and the channel from body surface to external base station. Such channels are defined as CM3 and CM4 for body area network in IEEE 802.15.6 standard [KPK12a] [tg610] [SLP12] [RFP12] [FDRe11]. In these particularly channels, geometrical relationship of the human body, target node and reference nodes lead

to various type of localization scenario. With chest mounted target sensor, whenever the reference node is located at the side or backside of the human, NLOS scenario can be raised in different scale resulting in relatively huge TOA ranging error [tg610]. Therefore, human body is an important source of TOA ranging error for indoor human tracking system.

The previous studies on behave of TOA ranging error in indoor environment provides typical and solid TOA ranging error model, separates the ranging error of LOS scenario and NLOS scenario [NA09a] [JHe11a] [AP06c] and presents statistical method to identify NLOS scenario [HP08]. However, these works fail to take the effects of human body into account and most of the latest TOA-based human tracking researches and applications are still based on the traditional ranging error model, suffering from the inaccuracy caused by the human body [Gp08] [STM11].

3.1.2 Chapter Outline

In this chapter, measurements have been conducted inside typical office environment with the target sensor mounted to the chest of human body. The TOA ranging error is observed to form a Gaussian distribution and the empirical measurement results have been analyzed from the perspective of system bandwidth, SNR, first path-to-power ratio (FNR) and geometrical relationship of human body, target node and reference nodes. Statistical model for the specific scenario has been built using bandwidth, SNR and geometrical information as parameters and the model coefficients have been properly worked out by curve fitting. The ranging error model is separated into LOS scenario and NLOS scenario and it also shows the minimum SNR required for successful localization. At the end of this chapter, the ranging error model has been validated.

3.2 Measurement Setup

In this section, we provide details of our measurement environment and necessary definitions for the rest of this Capter. Two major components of practical TOA-based indoor human tracking nodes are transceiver module that supports waveform transmission and MCU that runs the ranging and localization algorithms. To facilitate our measurement, a vector network analyzer (VNA) has been employed to accomplish the waveform transmission and record the channel profile. After that the channel profile will be parsed by post-processing program to get the TOA ranging.

3.2.1 System and Scenario

As shown in Figure 3.1, the measurement system employs a vector network analyzer (Agilent E8363), a pair of UWB antenna (Skycross SMT-3TO10M), low loss cables and a power amplifier (3-8GHz, 30db). The receiver (RX) antenna is used as target sensor, which is mounted to the middle of chest of human body with the height of 1.34 meters. The human involved remains standing posture during the measurement. The transmitter (TX) antenna is used as reference node and it is attached to a tripod with the same height as RX antenna.

During the measurement, S-parameter S_{21}, the transfer function of the channel, is measured by VNA in frequency domain with 1601 sample points. The received signal is transferred to time domain by inverse fast Fourier transform (IFFT) with a Hanning window applied to the time domain received channel profile to limit the sidelobe. The first peak can be detected by setting up proper threshold of the time domain signal strength and the propagation time of the first peak can be easily estimated. To guarantee the accuracy of the first path TOA, undesirable effects of the cables, the power amplifier, antennas and other system components

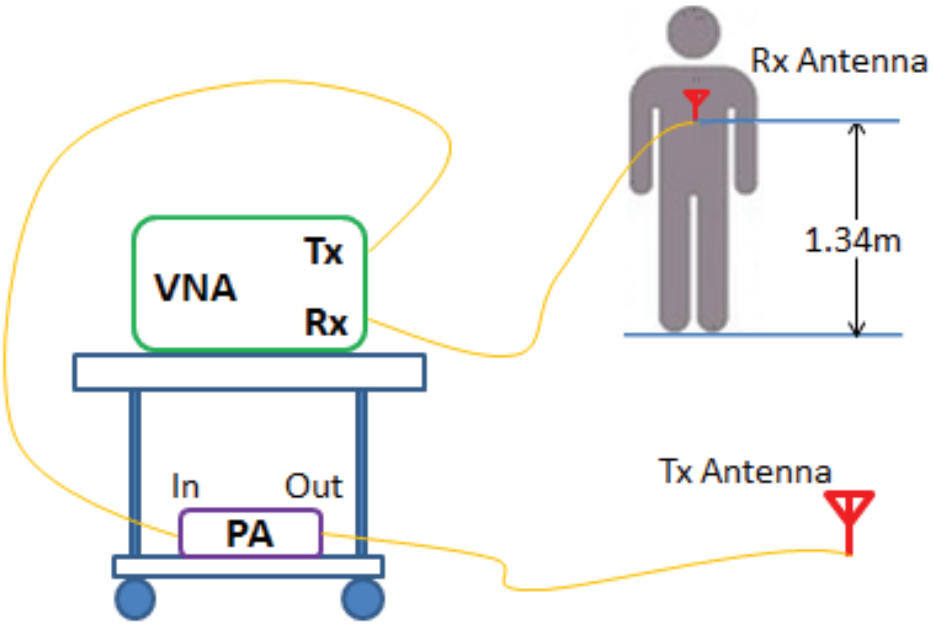

Figure 3.1: Measurement system including network analyzer, power amplifier, human body and antennas.

are removed through system calibration. Typical recorded channel profile has been shown in Figure 3.2 in which the first detected path above the threshold arrived at time τ. Therefore, the estimated distance between target sensor and reference node can be defined as $\hat{d} = \tau \times c$ where c is the speed of radio wave propagation in the free space.

The measurement was performed in Room 233 of Atwater Kent Laboratory, an office building located in Worcester Polytechnic Institute, Worcester, MA, US. As shown in Figure 3.3, this room is medium size with dimensions of approximately 18×12 meters and filled with desks, chairs, large windows and blackboards. The TX antenna is located near the wall and the distance between TX and RX antenna is fixed to 5m. TOA ranging error e can be then defined as:

$$e = \hat{d} - d, \tag{3.1}$$

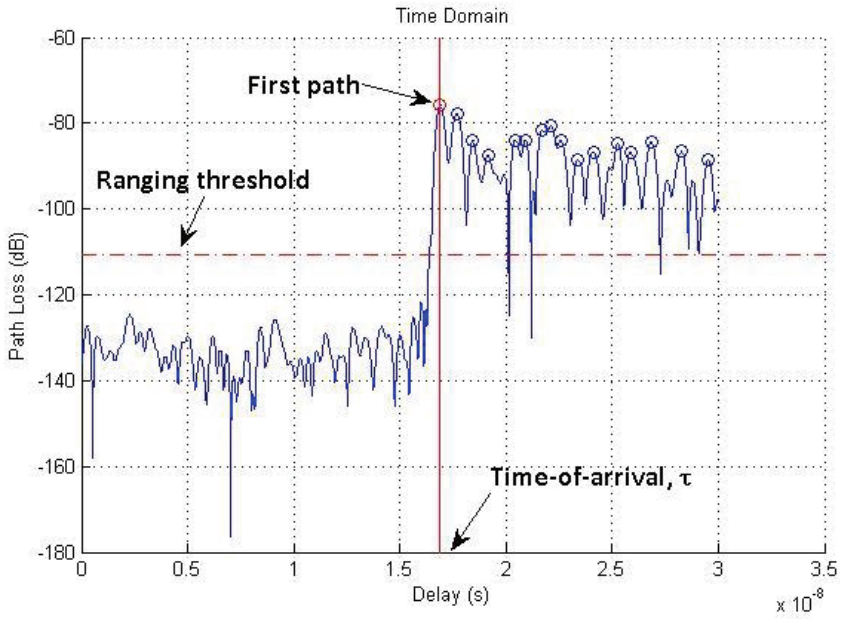

Figure 3.2: A sample of recorded time domain channel profile that shows the first path detection process.

where $\hat{d}$ is the distance estimation in our measurement and d is the actual distance, 5m.

3.2.2 Settings

Measurement cases can be described using a scenario-based approach. A measurement case set, denoted by:

$$Case = \{\theta, \mathrm{SNR}_{LOS}, W\}$$

is composed of a subset W which is the indoor human tracking system bandwidth, a SNR subset SNR_{LOS} which is the SNR without taking into account the effects of human body and an angle subset θ which represents the geometrical relationship of human body and TOA-based localization sensors. A specific case of our mea-

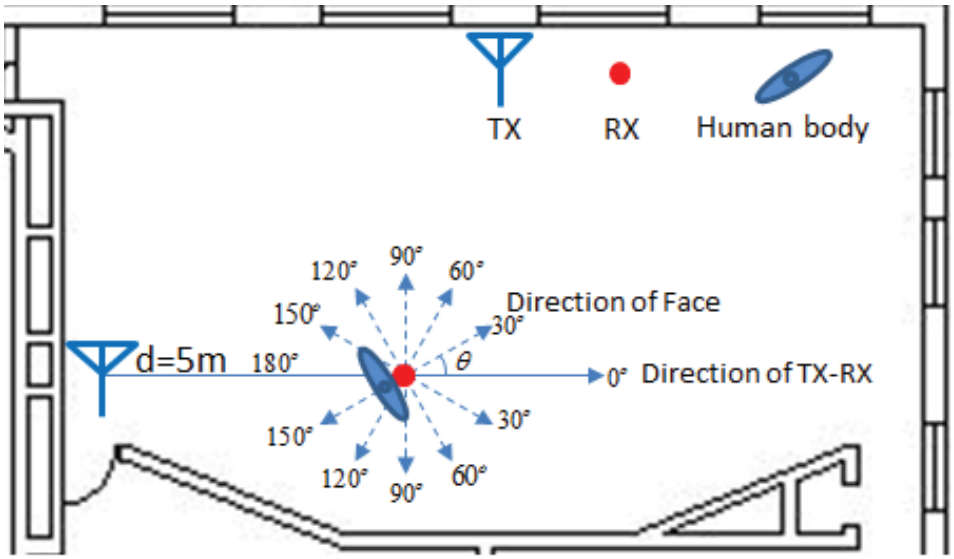

Figure 3.3: Measurement scenario with the angle θ defined as the horizontal angle between human facing direction and the TX-RX direction.

surement can be $Case = \{30^o, 62.0dB, 1GHz\}$. For each measurement case, the ranging error can be then defined as: $\hat{E}_{\theta,\mathrm{SNR}_{LOS},W}$. Over 600 TOA ranging errors are obtained in each case to guarantee the validity of the measurement result and definition and settings of three subsets are introduced as follow:

1) θ

As shown in Figure 3.3, the geometric relationship among human body, TX and RX is defined as the horizontal angle between the facing direction of the human body and the direction of TX-RX. Measurements are performed in every 30^o as shown in Figure 3.3 and the subset θ is given by:

$$\bar{\theta} = \{0^o, 30^o, 60^o, 90^o, 120^o, 150^o, 180^o\}$$

Measurement scenarios can be partitioned into LOS or NLOS scenario by whether the human body is blocking the direct line between TX and RX. To help classify

these two scenarios, we define the relationship between θ and physical scenario S as follow:

$$S = \begin{cases} NLOS, & \theta \in [0^o, 90^o) \\ LOS, & \theta \in [90^o, 180^o] \end{cases} \tag{3.2}$$

2) SNR

In the measurements, the transmit power P_{TX} of VNA has been set from 0 to -40 dBm by 10dBm per step to model the effect of human body on TOA ranging error in different SNR condition. In order to obtain SNR_{LOS}, RX antenna is attached to a tripod with the same height as TX antenna in the same position as depicted in Figure 3.3 and the pure background noise in the typical indoor environment of our measurement has been measured. SNR_{LOS} is then calculated by using P_{TX} and the background noise. The SNR subset SNR_{LOS} is defined as follows:

$$\bar{SNR}_{LOS} = \{71.5dB, 62.0dB, 52.4dB, 42.3dB, 32.4dB\}$$

3) W

Four popular UWB bandwidths ranging from 500MHz up to 5GHz are used in our measurements to analysis the effect of bandwidth on TOA ranging error for indoor human tracking. The system bandwidth subset W can be given by:

$$\bar{W} = \{5GHz, 3GHz, 1GHz, 500MHz\}$$

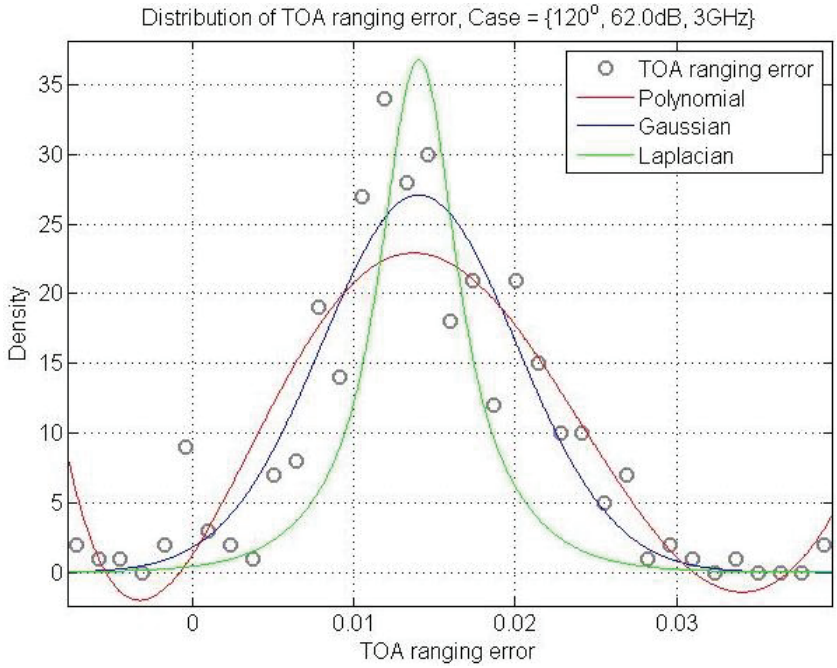

Figure 3.4: Sample distribution of TOA ranging error with PDF curve fitting, $Case = \{120^o, 62.0dB, 3GHz\}$.

3.3 Result Analysis

The general observation for our measurement is that the TOA ranging for every measurement case forms Gaussian distribution no matter in LOS scenario or NLOS scenario. The curve fitting result for sample result has been shown in Figure 3.4 in which the Gaussian PDF has been proved to be the best fit line.

3.3.1 Geometrical Relationship

To better understand the effect of geometrical relationship on TOA ranging error, the mean and variance of the Gaussian distribution have been further investigated. Figure 3.5 (a) and (b) shows the relationship between the mean and variance of TOA ranging error and the horizontal angle θ. As is mentioned in the previous sections, when $\theta \in [90^o, 180^o]$, we define it as the LOS scenario, which means the

human body is not blocking the direct line between TX and RX. In that scenario, both mean and variance of the TOA ranging error are relatively stable, indicating that the horizontal angle θ has little effect on the TOA ranging error distribution because the direct path always exists and the first path we observed in the time domain channel profile can be regarded as the direct path itself.

In the pre-defined NLOS scenario where $\theta \in [0^o, 90^o)$, dramatic change of both the mean and variance can be found and both mean and variance of the TOA ranging error decrease with the increment of angle θ. As (a) shows, when the TX is located in the center of human torso and RX is located at the surface of middle chest at the same height of TX, the software simulation using FDTD method proved that the pathloss of the TX-RX link is as large as 56.2dB. Based on that result, the total penetration loss of human body can be over 80dB [QWW09]. With such a huge attenuation, the direct path that penetrates the human body will be no longer detectable and the creeping wave can be regarded as the dominant of the TOA ranging error.

Figure 3.6 (b), (c) and (d) shows the creeping wave around human body with various value of horizontal angle θ. The creeping wave initiates from the TX and travels along the dual direction around the human body. With the increment of angle θ, the length of the blue ray decreases while the length of the red ray increases. As a result, the blue ray turns out to be less attenuated and becomes the first arrival path at the RX. Since [JCP12] argues that for every radian of angle θ there will be 18dB more attenuation and around 0.4ns delay of the creeping wave, with larger angle θ the TOA ranging error is supposed to be smaller. The above discussion reasonably explained the measurement result shown in Figure 3.5 (a) and (b).

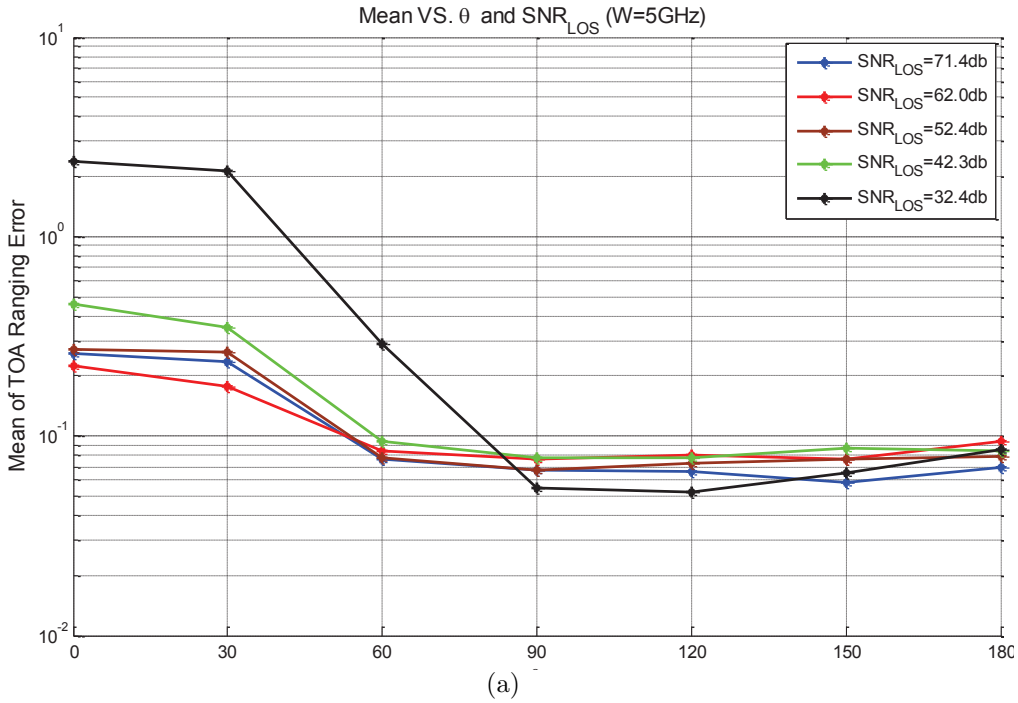

(a)

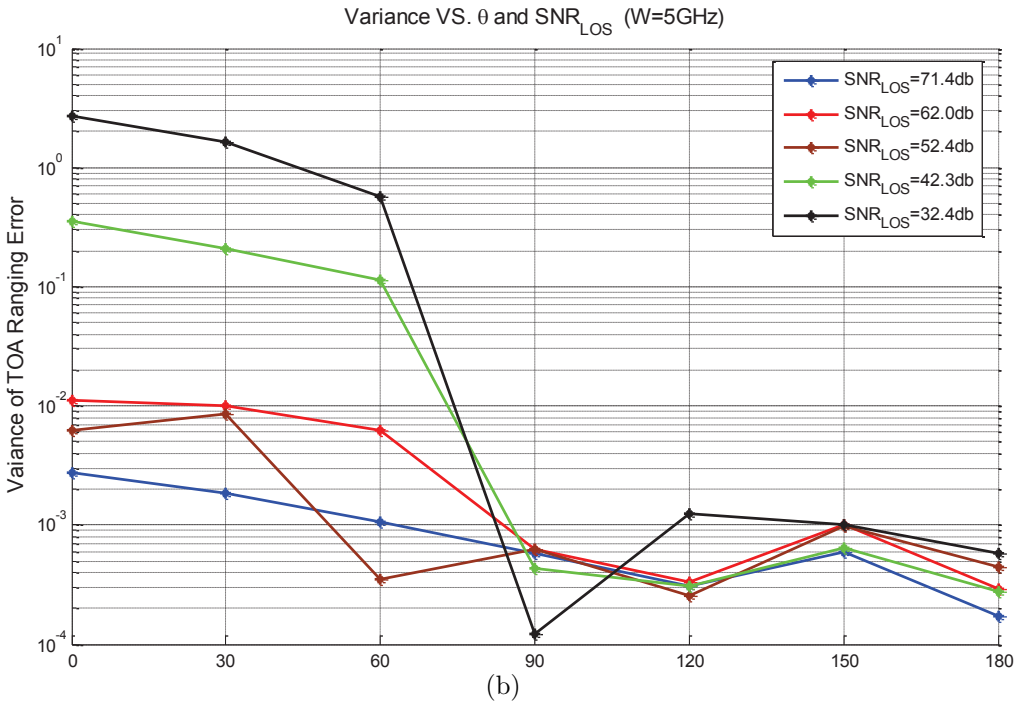

(b)

Figure 3.5: Effect of θ and SNR_{LOS}. (a):Variation of the mean of TOA ranging error. (b):Variation of the variance of TOA rangign error.

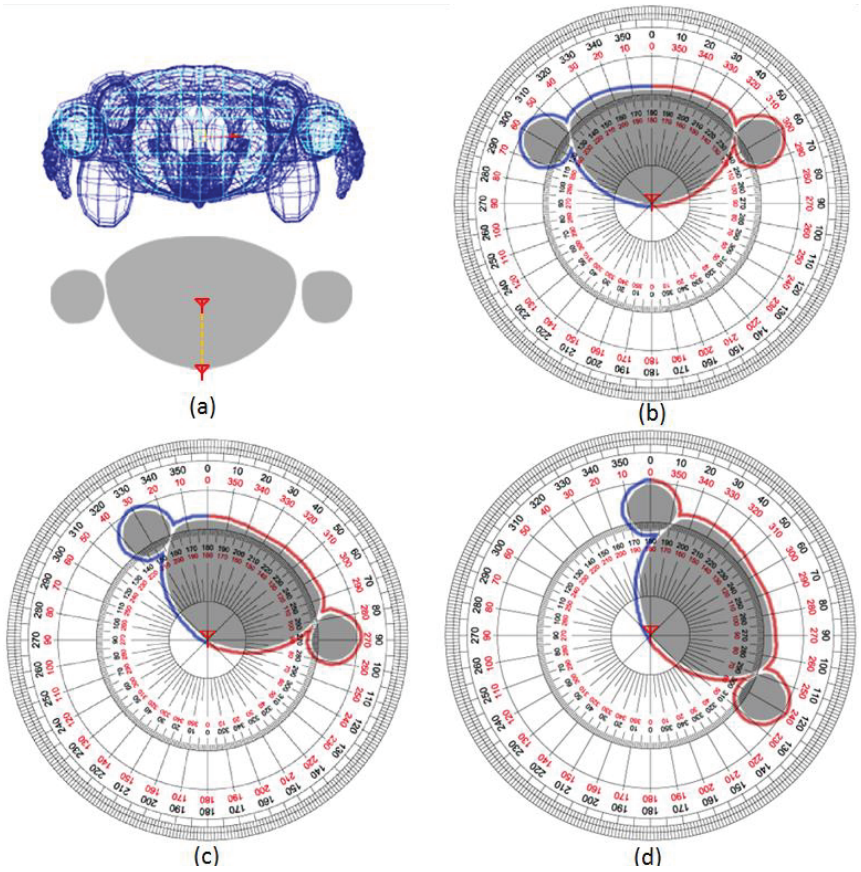

Figure 3.6: Sketch of creeping wave phenomenon around human body. (a): Section of a male adult torso from 3D human body model. (b): creeping wave phenomenon when $\theta = 0^o$. (c): creeping wave phenomenon when $\theta = 30^o$. (d): creeping wave phenomenon when $\theta = 60^o$.

3.3.2 Effect of Bandwidth

Bandwidth is a critical feature to the precision of TOA based localization system. To further analyze the effect of bandwidth on TOA ranging error, additional measurement has been conducted at different system bandwidth and the subset W has been expanded to:

$$\bar{W}_{expanded} = \{50MHz, 100MHz, 200MHz, 300MHz,$$

$$500MHz, 1GHz, 1.2GHz, 1.5GHz, 2GHz, 2.5GHz,$$

$$3GHz, 3.5GHz, 4GHz, 4.5GHz, 5GHz\}$$

As we expected, when the bandwidth drops, both mean and variance of TOA ranging error increase. Figure 3.7 shows that given 5GHz system bandwidth, the mean of ranging error can be limited within 0.1934 meters while given only 50MHz bandwidth, the mean error raises up to several meters. When the bandwidth is larger than 1GHz, the order of magnitude of variance remains under 0.2 meter. However, for 50MHz bandwidth, the variance dramatically runs up to more than 5 meters.

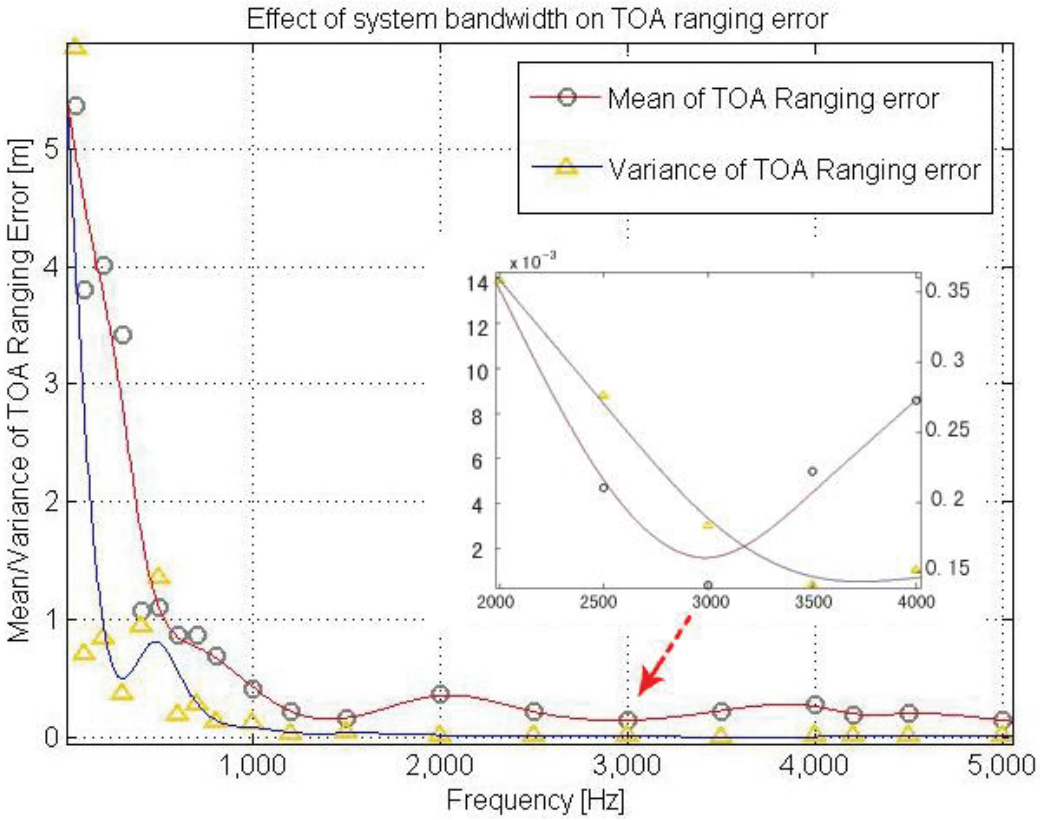

Figure 3.7: Effect of system bandwidth on TOA ranging error. Origin frequency band ranges from 50MHz to 5GHz and the 2GHz-4GHz band has been zoomed in.

The empirical experiment result shows that there exists a threshold of bandwidth over which the increment of bandwidth no longer benefits the localization performance. That threshold is investigated by zooming in the 2GHz to 4GHz frequency band. As can be seen in Figure 3.7, at approximately 3GHz, we obtain the minimum value of mean of TOA ranging error, while at around 3.5GHz, the minimum variance of the TOA ranging error can be observed. For bandwidth more than 3.5GHz, performance can be hardly ever further improved by providing larger bandwidth.

3.3.3 Effect of Transmit Power

As can be seen from Figure 3.5 (a) and (b), the signal to noise ratio also has a strong influence on the TOA ranging performance. Both mean and variance increase with the decrement of SNR. Figure 3.5 also shows that, in 500MHz, the worst bandwidth option in subset W, the mean of TOA ranging error exceeds 1.4 meters and the variance even also goes beyond 1.65 meters.

Apart from SNR, first-peak-to-noise-ratio (FNR) is another significant metric to evaluate the performance of TOA-based human tracking systems due to the fact that TOA estimate thoroughly relies on the detection of direct path. Particularly in the NLOS scenario, if the direct path is attenuated but still detectable, its referred to as detected-direct-path (DDP) scenario in which the ranging error remains acceptable even though it slightly increases. On the contrary, if the direct path completely disappears and becomes undetectable, the first peak above threshold will be regard as the direct path, resulting in a huge undetected-direct-path (UDP) ranging error for NLOS scenario.

Figure 3.8 shows the relationship between SNR, FNR and angle in NLOS scenario. Mean of ranging error has been added to the figure for better illustration. As

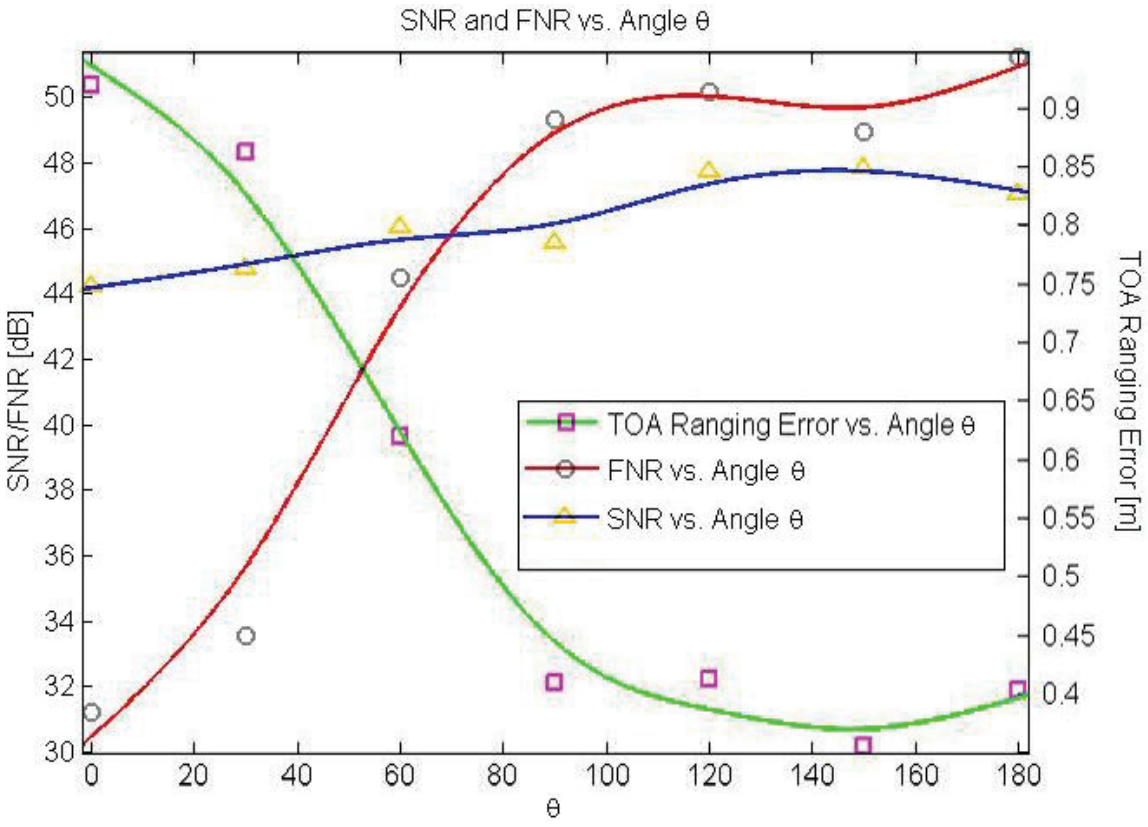

Figure 3.8: Relationship between SNR, FNR and angle θ. TOA ranging error has been provided as a reference.

can be seen from the figure, mean error reaches the maximum value when human body completely block the direct path and at that time, the largest decrement of power of first path (FNR) is no more than 22dB. Since our threshold is defined much lower than the expected minimum power of first arrival path and previous research shows that the UWB signal suffers from approximately 80dB [QWW09] attenuation when penetrating the human body we conclude that the direct path that penetrate the human body is not detectable and the creeping wave along the surface of human body is the detected first path.

3.4 Modeling TOA Ranging Error for Chest Mouted Sensors

The previous section provides general explanation of the effect of human body on the indoor TOA based human tracking system. However, to facilitate the design and evaluation of practical applications, quantitative explanation is required. To fulfill the demand, we build mathematical model for the effect of human body on TOA ranging error.

3.4.1 Regression Fitting

Based on the above discussion, TOA ranging error can be defined as the combination of multipath error and the NLOS error which includes the effect of penetration loss and creeping wave. As a result, the TOA ranging error is given by:

$$e = \epsilon_M + \delta(P_{NLOS}(\theta) - 1) \times \epsilon_{NLOS} \tag{3.3}$$

where ϵ_M is multipath error, ϵ_{NLOS} is NLOS error. $\delta(x)$ is the impulse function, given by:

$$\delta = \begin{cases} 1, & x = 0 \\ 0, & x \neq 0 \end{cases} \tag{3.4}$$

According to (3.2), probability P_{NLOS} is employed to classify the LOS and NLOS scenario, which can be defined as:

$$P_{NLOS}(\theta) = \begin{cases} 1, & \theta \in [0^o, 90^o) \\ 0, & \theta \in [90^o, 180^o] \end{cases} \tag{3.5}$$

1) ϵ_M

According to (3.3), in the LOS scenario, the TOA ranging error equals to multipath error:

$$e_{LOS} = \epsilon_M \tag{3.6}$$

To model the multipath error for body mounted sensors, the measured data of LOS scenario ($\theta \in [90^o, 180^o]$) are used to determine the distribution parameters. Our measurement result shows that for each bandwidth employed in the subset W, the ranging error forms a Gaussian distribution. Therefore the multipath error can be modeled as:

$$\epsilon_M = G(\mu_{M,W}, \sigma^2_{M,W}) \tag{3.7}$$

where G is a Gaussian random variable with mean $\mu_{M,W}$ and variance $\sigma^2_{M,W}$. The values of $\mu_{M,W}$ and $\sigma^2_{M,W}$ varies according to the system bandwidth and typical values have been listed in Table I.

2) ϵ_{NLOS}

According to (3.3), In the NLOS scenario, the TOA ranging error ϵ_{NLOS} can be given by:

$$\epsilon_{NLOS} = e_{NLOS} - \epsilon_M \tag{3.8}$$

where e_{NLOS} is the ranging error. Based on our previous observation, both e_{NLOS} and ϵ_M correspond with Gaussian distributions. Therefore, e_{NLOS} can be also modeled as a Gaussian random variable, given by:

$$\epsilon_{NLOS} = G(\mu_{NLOS}, \sigma^2_{NLOS}) \tag{3.9}$$

where the mean and variance of the random variable, μ_{NLOS} and σ^2_{NLOS} can be given by:

$$\mu_{NLOS} = \mu_{e_{NLOS}} - \mu_{LOS} \tag{3.10}$$

$$\sigma^2_{NLOS} = \sigma^2_{e_{NLOS}} - \sigma^2_{LOS} \tag{3.11}$$

where $\mu_{e_{NLOS}}$ is the mean of e_{LOS} and $\sigma^2_{e_{NLOS}}$ is the variance of e_{LOS}. As can be seen from Fig. 5, the plot of both μ_{NLOS} and σ^2_{NLOS} in our measurements result share a similar trend with the function $\cos^a(\theta)$. Concequentely, after mathematical work, for given W and SNR_{LOS}, we model both μ_{NLOS} and σ^2_{NLOS} as a linear function of $\cos^3(\theta)$ as follows:

$$\mu_{NLOS} = k_1 \times \cos^3\theta \tag{3.12}$$

$$\sigma^2_{NLOS} = k_2 \times \cos^3\theta \tag{3.13}$$

where k_1 and k_2 are the slope of the linear functions. Figure 3.9 shows the fitting results of e_{LOS} and $\sigma^2_{e_{NLOS}}$ versus θ when $W = 5GHz$. As depicted in Fig. 9, k_1 and k_2 increase as SNR_{LOS} declines, indicating that the effects of body-caused NLOS error is relatively severe in low SNR conditions. We believe that in low SNR situation, path detection is rather challenging because of the difficulty in properly setting up a threshold and detection failure occurs more frequently. The coefficients k_1 and k_2 can be then modeled as a rational function of SNR_{LOS} as follows:

$$k_1 = \frac{a_W}{\mathrm{SNR}_{LOS} - \mathrm{SNR}_{Thrd,W}} \tag{3.14}$$

$$k_2 = \frac{b_W}{\mathrm{SNR}_{LOS} - \mathrm{SNR}_{Thrd,W}} \tag{3.15}$$

where a_W, b_W and $\mathrm{SNR}_{Thrd,W}$ are the coefficients depend on system bandwidth W.

One thing worth mentioning is that $\text{SNR}_{Thrd,W}$ shows the threshold of SNR_{LOS} for TOA ranging in body-caused NLOS scenario. If the SNR goes below the threshold in our model, reception faliaure of the reference nodes dramatically increases and peak detection becomes very difficult. Values of a_W, b_W and $\text{SNR}_{Thrd,W}$ are calculated by curve fitting and shown in Table 3.4.2. Figure 3.10 shows the fitting results of k_1 and k_2 versus SNR_{LOS} when system bandwidth $W = 5GHz$.

If we put together equation (12), (13), (14) and (15), ϵ_{NLOS} can be finally modeled as:

$$\epsilon_{NLOS} = G(\mu_{NLOS,W}, \sigma^2_{NLOS,W}) \tag{3.16}$$

where

$$\mu_{NLOS,W} = \frac{a_W}{\text{SNR}_{LOS} - \text{SNR}_{Thrd,W}} \times \cos^3(\theta) \tag{3.17}$$

$$\sigma^2_{NLOS,W} = \frac{b_W}{\text{SNR}_{LOS} - \text{SNR}_{Thrd,W}} \times \cos^3(\theta) \tag{3.18}$$

3.4.2 General Model

According to analysis and the fitting results above, the overall model of TOA ranging error for body mounted sensors is given by:

$$e = \epsilon_M + \delta(P_{NLOS} - 1) \times \epsilon_{NLOS}$$

$$= G(\mu_{M,W}, \sigma^2_{M,W}) + \delta(P_{NLOS} - 1) \times G(\mu_{NLOS,W}, \sigma^2_{NLOS,W}) \tag{3.19}$$

where $\mu_{NLOS,W}$ and $\sigma^2_{NLOS,W}$ are defined in (3.17) and (3.18). The values of all the coefficients of the model have been shown in Table 3.4.2.

Table 3.1: Coefficients for the TOA ranging error model for chest mounted sensors.

W(GHz)	$\mu_{M,W}$(m)	$\sigma^2_{M,W}$(m)	a_W	b_W	$\text{SNR}_{Thre,W}$(dB)
5	0.010	0.005	5.10	5.49	30.4
3	0.009	0.001	3.98	6.69	30.4
1	0.072	0.058	6.21	11.76	29.0
0.5	0.138	0.143	14.69	10.62	27.5

3.4.3 Model Validation

Validation of the general model has been provided in Figure 3.11. In Figure 3.11 (a), the complementary CDF of the empirical measured TOA ranging error of LOS scenario has been compared with the CDF of software simulated ranging error given system bandwidth of 3GHz. In Figure 3.11 (b), we compared the TOA ranging error of NLOS scenario with the software simulated ranging errors in $Case = \{0^o, 62.0dB, 3GHz\}$. Both comparison shows that the simulated data has close agreement with the empirical data and we can therefore, prove the validity of our general model of TOA ranging error.

3.5 Summary

In this chapter, we introduce a TOA ranging error model for body mounted sensors based on the measurements in a typical office building. This model separates the ranging error into multipath error and NLOS error, which is caused by the penetration loss of the human body and the creeping wave around human body. Both multipath error and NLOS error are modeled as a Gaussian variable. The distribution of multipath error is related to bandwidth of the system while the distribution of NLOS error is related to the angle between the human facing direction and the direction of TX-RX, SNR and bandwidth of the system, which clearly shows the effects

of human body on TOA ranging. The comparison between the empirical ranging error and simulated ranging error depicts close agreement, proving the validity of the TOA ranging error for body mounted sensors.

The contribution of this chapter is three-folded. First and foremost, this chapter is the first one that considers the effect of human body on TOA ranging error of indoor human tracking system. Secondly, creeping wave phenomenon has been discussed in the result analysis section. Last but not the least, it is the first time that the horizontal angle θ has been selected as a parameter instead of the frequently used distance between TX and RX in the literature. We are currently at the initial phase of this research and our ultimate goal is to fully understand the effect of human body and eliminate the inaccuracy raised by human body. Since with a chest mounted sensor, the human body can be regarded as a symmetric structure and the range of angle θ can be limited within 180^o. Whenever the sensors are attached to human wrist and ankle or even located in the pocket, the symmetry will no longer exist. The scenario with wrist mounted sensors has been presented in next chapter.

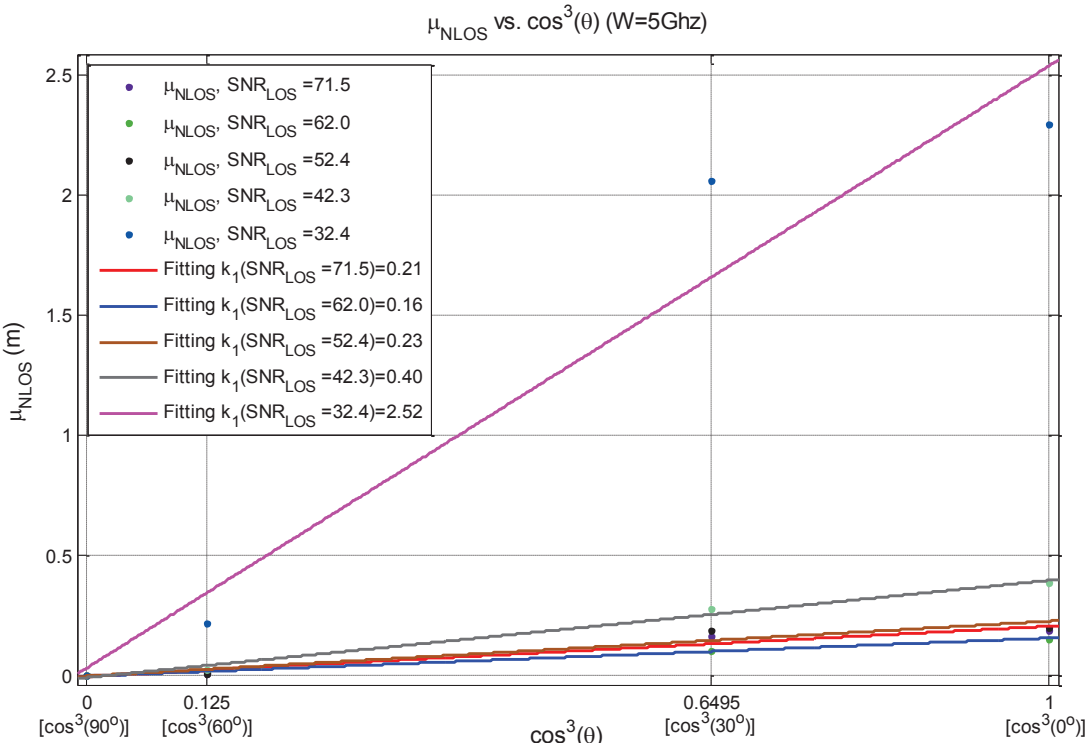

(a)

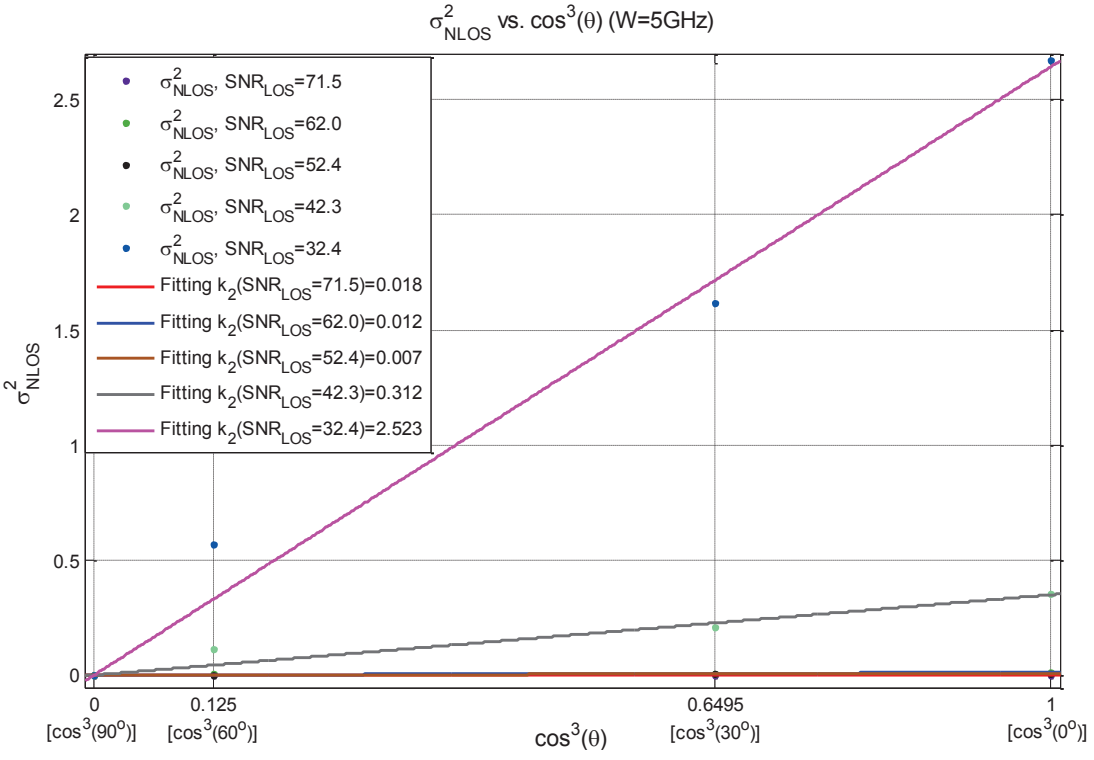

(b)

Figure 3.9: Linear fitting results of μ_{LOS} and σ^2_{LOS} vs. $\cos^3(\theta)$. (a): μ_{LOS} vs. $\cos^3(\theta)$. (b): σ^2_{LOS} vs. $\cos^3(\theta)$.

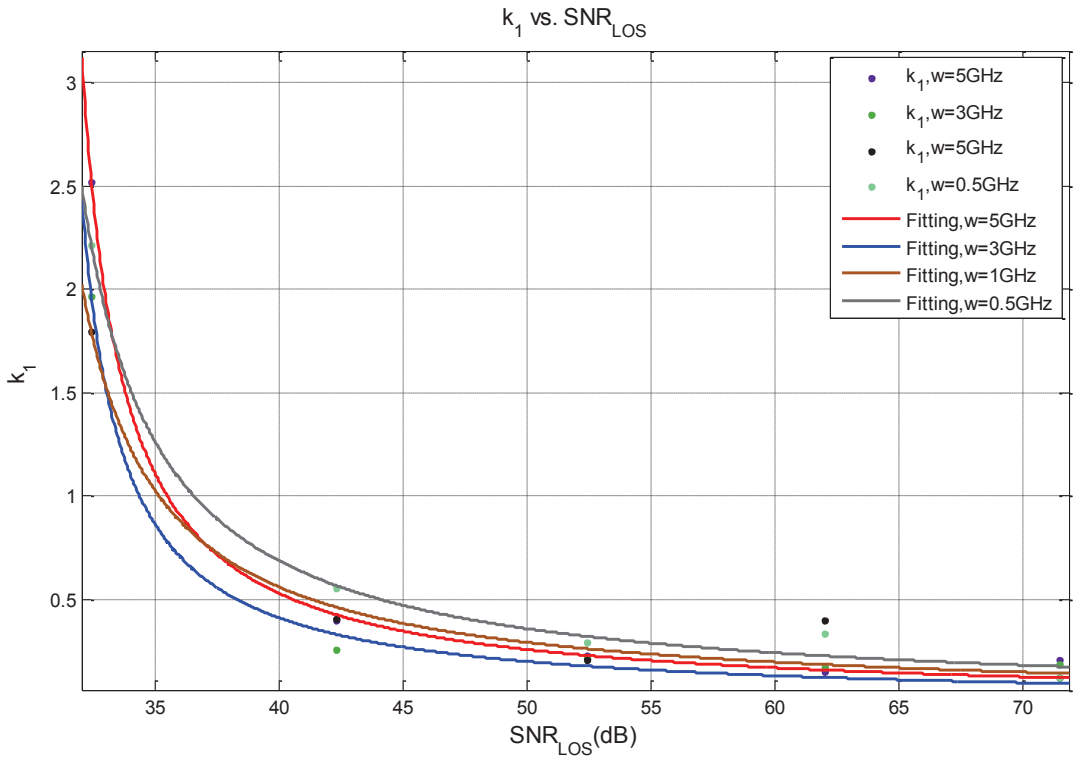

(a)

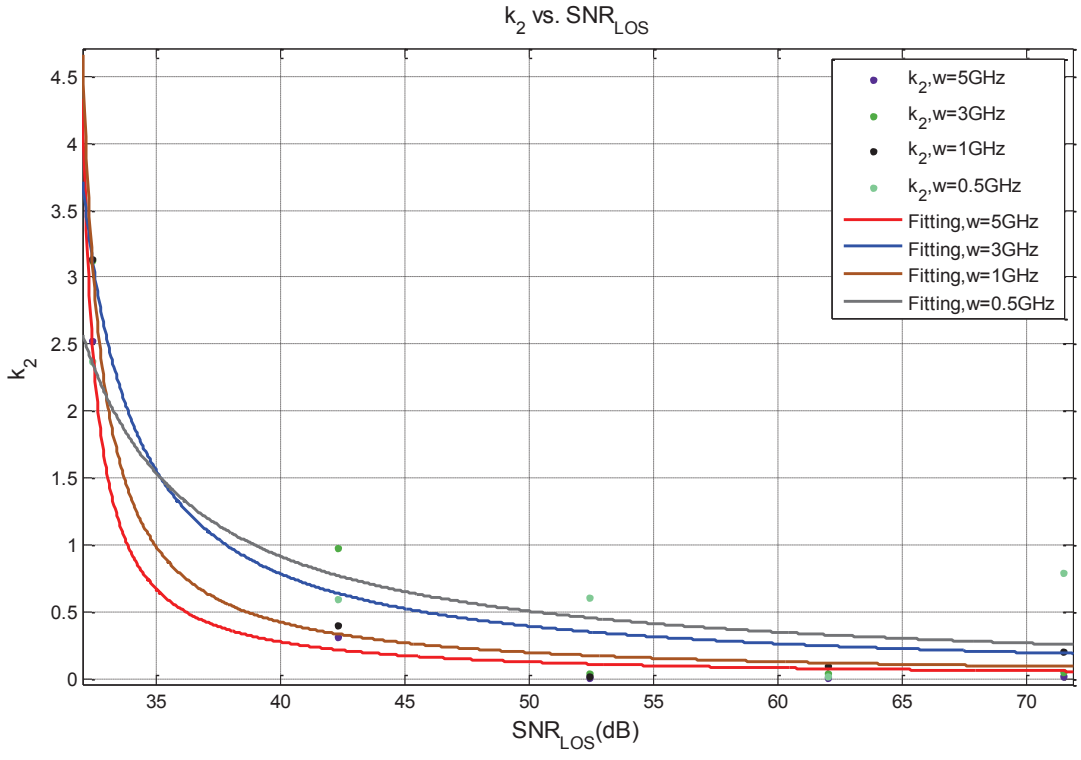

(b)

Figure 3.10: Rational fitting results of k_1 and k_2 vs. SNR$_{LOS}$. (a): k_1 vs. SNR$_{LOS}$. (b): k_2 vs. SNR$_{LOS}$.

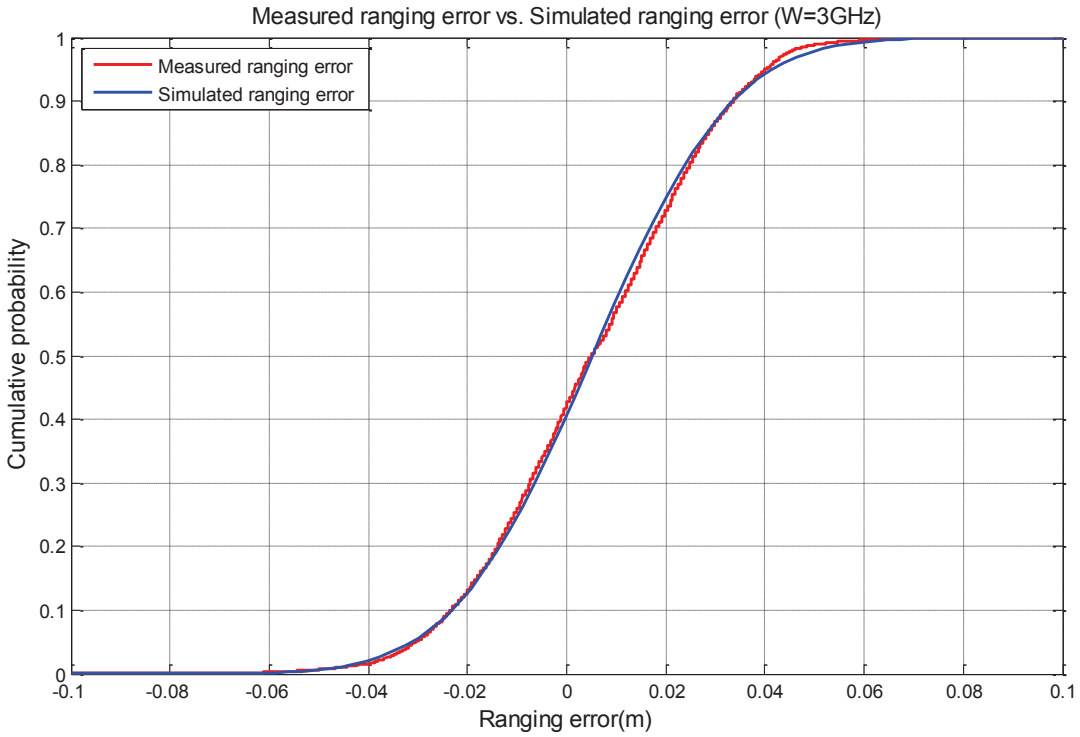

(a)

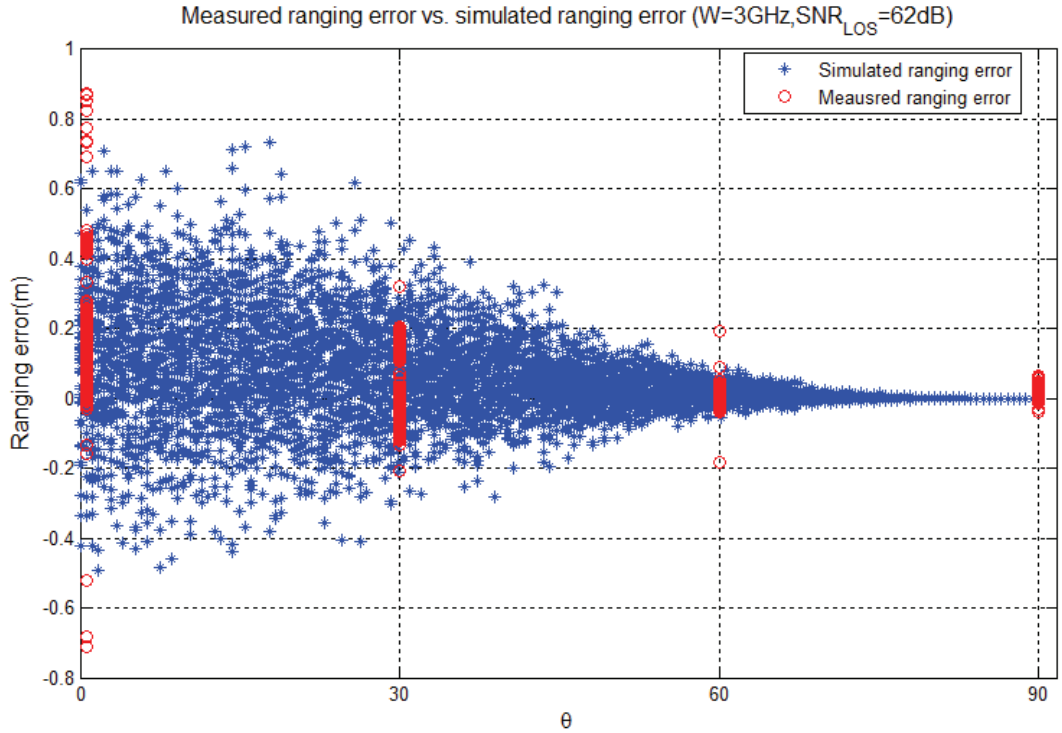

(b)

Figure 3.11: Comparison between empirical measurement result and software simulation result using the model presented above. (a): Comparison of CDF in LOS scenario. (b): Comparison of TOA ranging error in NLOS scenario, $Case = \{0^o, 62.0dB, 3GHz\}$.

Chapter 4

Modeling the TOA Ranging Error for Wrist Mounted Sensors

4.1 Introduction

The indoor human tracking industry has a trend to merge with the body area network (BAN) due to the fact that for human tracking systems, target nodes are often attached to the surface of human body and the radio propagation channel between body mounted sensors and exterior base stations (BSs) are delicately defined as CM4 for body area network in IEEE 802.15.6 standard [KPK12b] [tg610]. Previous research shows that when target nodes are attached to body surface, none line-of-sight (NLOS) scenario can be produced by the human body, resulting in severe error in TOA estimation [JHP12a] [KPK12b]. Therefore, human body can be regarded as one of the major source for TOA ranging error when the body mounted sensors are involved. General behavior of TOA ranging error in indoor localization has been studied in [NA09b] [JHe11b] [AP06a], but these works fails to mention the effect of human body. Our previous work [JHe11b] takes the influence of human body into

consideration but the position of body mounted sensor is limited to the middle of human chest.

In this chapter, measurements have been conducted inside typical office environment with the target sensor mounted to human wrist. The TOA ranging error is observed to form a Gaussian distribution and analysis has been applied to the empirical measurement results from the perspective of geometrical relationship, system bandwidth, signal to noise ratio (SNR) and first-path to noise ratio (FNR). A statistical model for the specific scenario has been built using bandwidth, geometrical relationship and SNR as parameters and coefficients are properly worked out by curve fitting. At the end of this chapter, we validate our model and compare it with the model for chest mounted scenario in previous chapter.

4.2 Measurement Setup

4.2.1 System and Scenario

To measure the behavior of target node and base stations, a vector network analyzer has been employed in our measurement system. Two UWB used omnidirectional antennas have been connected to both transmit and receive port of the network analyzer through low loss RF cables and a power amplifier has been added at the transmitter (TX) port of network analyzer to achieve better SNR at the receiver (RX) side. As is shown in Figure 4.1, the receiver antenna is attached to the left wrist of human body at the height of 1.06m which is the commonposition for smart watch or smart phone in the trouser pocket. These devices are often used as the coordinator in body area network. The human involved in this measurement remains standing posture throughout the measurement. Transmitter antenna used as base station is fixed to a tripod with the same height as the receiver antenna.

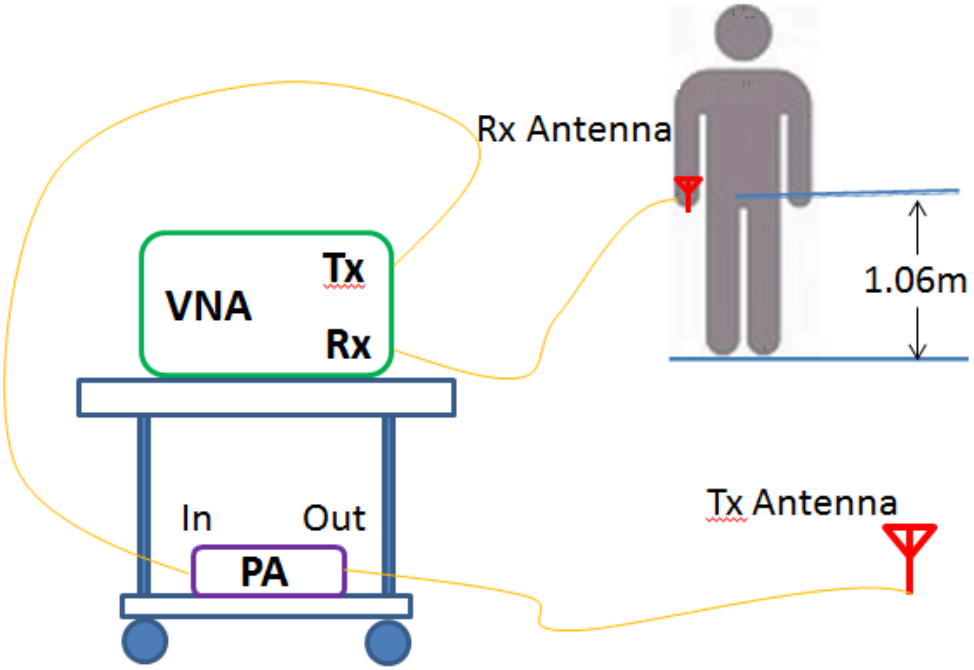

Figure 4.1: Measurement system including network analyzer, power amplifier, human body and antennas.

The channel forward gain S-parameter S21 is measured by the network analyzer by 1601 sample points in frequency domain and then Hanning windows are applied to the logged frequency domain profile in order to limit side lobes. After that, inverse fast Fourier transform (IFFT) is executed to transfer the frequency domain profile to time domain. By setting up proper threshold, the propagation time of first detectable peak is logged for TOA estimation and all of the undesirable effects from devices are eliminated through system calibration.

The measurement is conducted in Room 233, Atwater Kent Building, Worcester Polytechnic Institute, Worcester MA, which is a typical medium size office environment with dimension of approximately 18×12 meters. TX antenna is located 5 meters away from the body mounted RX antenna and the TOA ranging error e is defined as the difference between estimated distance $\hat{d}$ and the actual distance d in

(1):

$$\epsilon = \hat{d} - d \tag{4.1}$$

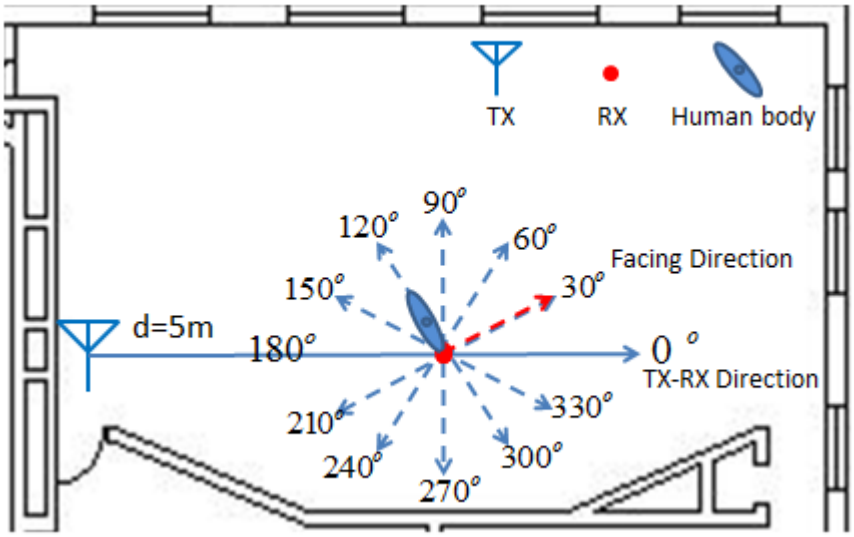

Figure 4.2: Measurement scenario with the angle θ defined as the horizontal angle between human facing direction and the TX-RX direction.

4.2.2 Settings

As can be seen from Figure4.2, the three critical metric of our measurements are system bandwidth W, the ratio of signal to background noise SNR_{LOS}, and the angle θ between the human facing direction and TX-RX direction. The human facing direction changes every 30 degrees and the LOS and NLOS scenarios are identified by the angle θ. From 90 degrees to 270 degrees, we define it as the NLOS scenario in which at least part of human body is located in between the TX and RX, blocking the direct line-of-sight while the other half cases are defined as LOS scenario. The mathematical expression can be listed as follow:

$$W = \{5GHz, 3GHz, 1GHz, 0.5GHz\}$$

$$SNR_{\text{LOS}} = \{72.5dB, 63.1dB, 52.9dB, 43.2dB, 32.8dB\}$$

$$\theta = \{0^o, 30^o, 60^o, 90^o, ...300^o, 330^o\}$$

$$S = \begin{cases} NLOS, & \theta \in [0^o, 180^o) \\ LOS, & \theta \in [180^o, 330^o] \end{cases} \tag{4.2}$$

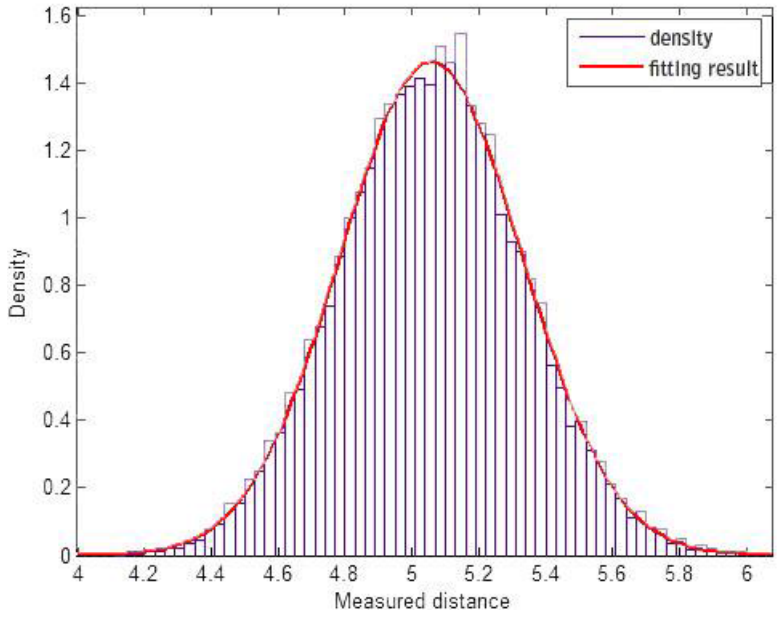

Figure 4.3: Sample distribution of TOA ranging error with PDF curve fitting, $Case = 90^o, 63.1dB, 5GHz$.

4.3 Result Analysis

Based on the parameters defined in the previous section, the TOA ranging error can be predefined as $\hat{E}_{\theta,SNR_{\text{LOS}},W}$. In each test case, at least 600 set of TOA estimations are obtained and the ranging errors are properly worked out. The first observation is that for every test case, the TOA ranging error forms a Gaussian distribution no matter in LOS or NLOS scenario. Typical result for single test case is shown in Figure 4.3.

4.3.1 Geometrical relationship

After obtained the Gaussian distribution result, we further analysis the mean and variance of the distribution for each test case. As can be seen from Figure 4.4, the value of mean and variance of each test case varies a lot and clear distinction exists between LOS and NLOS scenarios. In LOS scenario, both the mean and variance fluctuate in a relatively small scale while in NLOS scenario, dramatic change of both the mean and variance can be observed with different geometrical relationship.

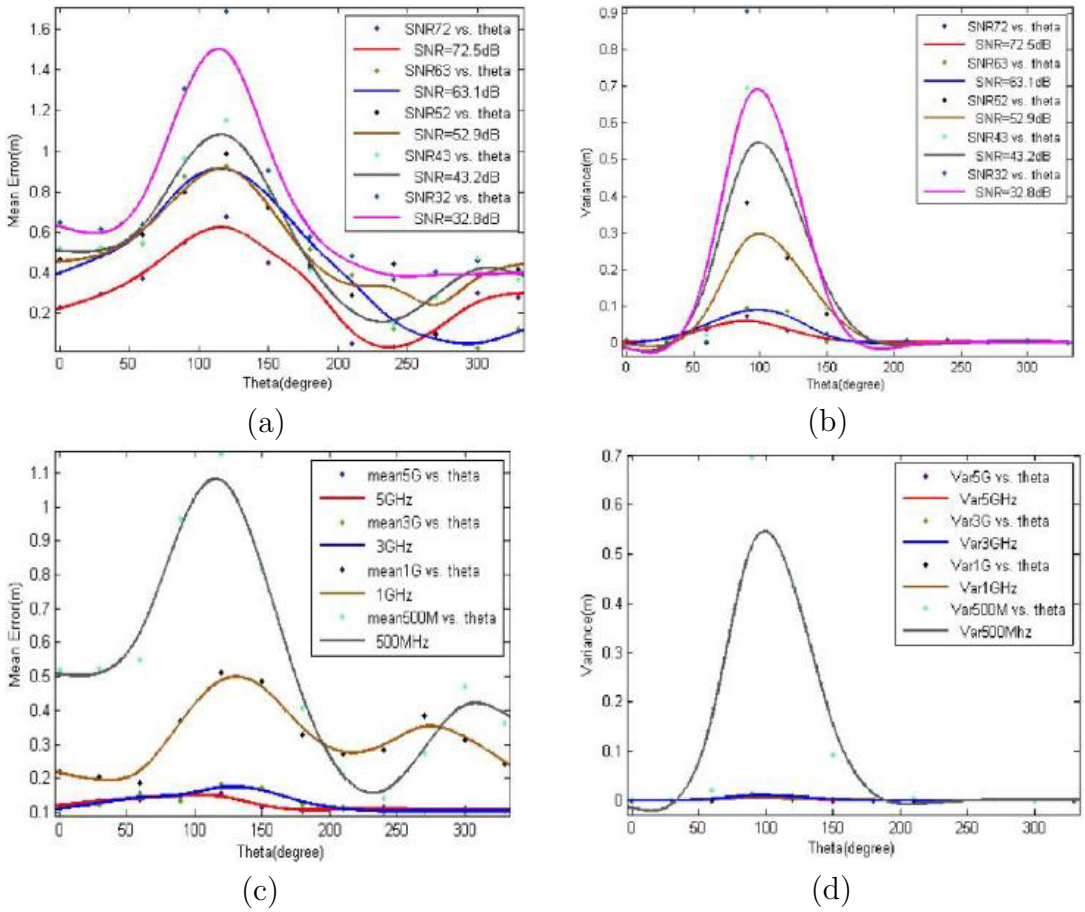

Figure 4.4: Measurement results. (a) and (b): Mean and Variance of TOA ranging error with respect to SNR. (c) and (d): Mean and variance of TOA ranging error with respect to system bandwidth.

4.3.2 Effect of Bandwidth

Bandwidth is a critical feature to the precision of TOA based localization system. In order to provide enough bandwidth, our measurement starts from 5GHz and goes all the way down to 50MHz. As we expected, when the bandwidth drops, both mean and variance of TOA ranging error increase. Figure 4.4 shows that given 5GHz system bandwidth, the mean of ranging error can be limited within 0.159 meters while given only 500MHz bandwidth, the mean error raises up to over 1 meter. When the bandwidth is larger than 1 GHz, the order of magnitude of variance remains under 0.01 meter. However, for 500MHz bandwidth, the variance dramatically runs to more than 0.5 meters.

The empirical experiment result shows that there exists a threshold of bandwidth over which the increment of bandwidth no longer benefits the localization performance. That threshold is investigated by zooming in the 3GHz to 4.2GHz frequency span. As can be seen in Figure 4.5, at approximately 3.8GHz, we obtain the minimum value of mean and variance for the TOA ranging error and for bandwidth more than 3.8GHz, performance cannot be further improved.

4.3.3 Effect of Transmit Power

The signal to noise ratio also has a strong influence on the TOA ranging performance. Both mean and variance increase with the decrease of SNR. As can be seen from Figure 4.4, in 500MHz, the worst bandwidth case of our measurement, the mean of TOA ranging error exceeds 1.6 meters and the variance also goes beyond 0.9 meters.

Apart from SNR, first-peak-to-noise-ratio (FNR) is also significantly important for TOA-based localization due to the fact that TOA estimate thoroughly relies on the detection of direct peak. Particularly in the NLOS scenario, if the direct path

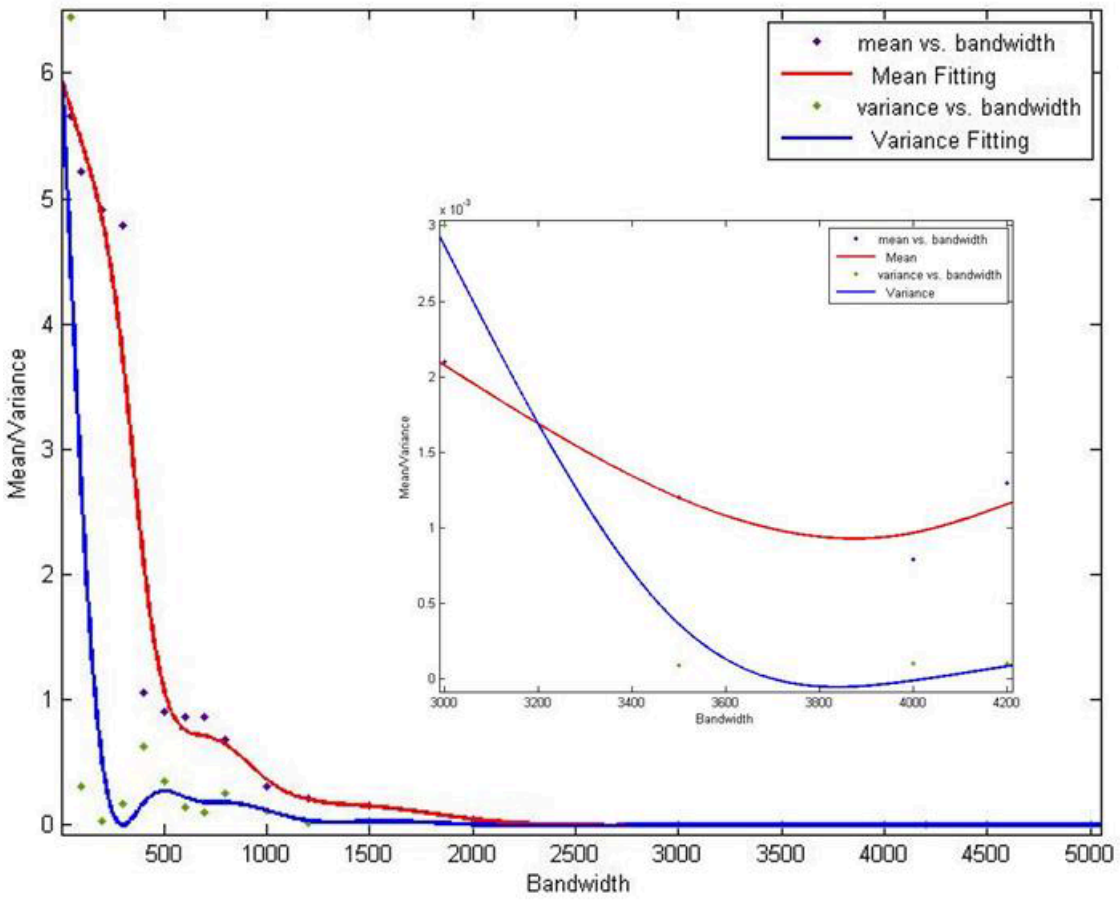

Figure 4.5: Effect of system bandwidth on TOA ranging error. Origin frequency band ranges from 50MHz to 5GHz and the 2GHz-4GHz band has been zoomed in

is attenuated but still detectable, its referred to as detected-direct-path (DDP) scenario in which the ranging error remains acceptable even though it slightly increases. On the contrary, if the direct path completely disappears and becomes undetectable, the first peak above threshold will be regard as the direct path, resulting in a huge undetected-direct-path (UDP) ranging error for NLOS scenario.

Figure 4.6 shows the relationship between SNR, FNR and angle θ in NLOS scenario, mean of ranging error has been added to the figure for better illustration. As can be seen from the figure, mean error reaches the maximum value when human body completely block the direct path and at that time, the largest decrement of

power of direct path (FNR) is no more than 17dB. Since our threshold is defined much lower than the minimum power of direct path and previous research shows that the UWB signal suffers from approximately 80dB attenuation when penetrating the human body we conclude that the direct path still exists and the radio signal propagates along the surface of human body in the pattern of creeping wave [12].

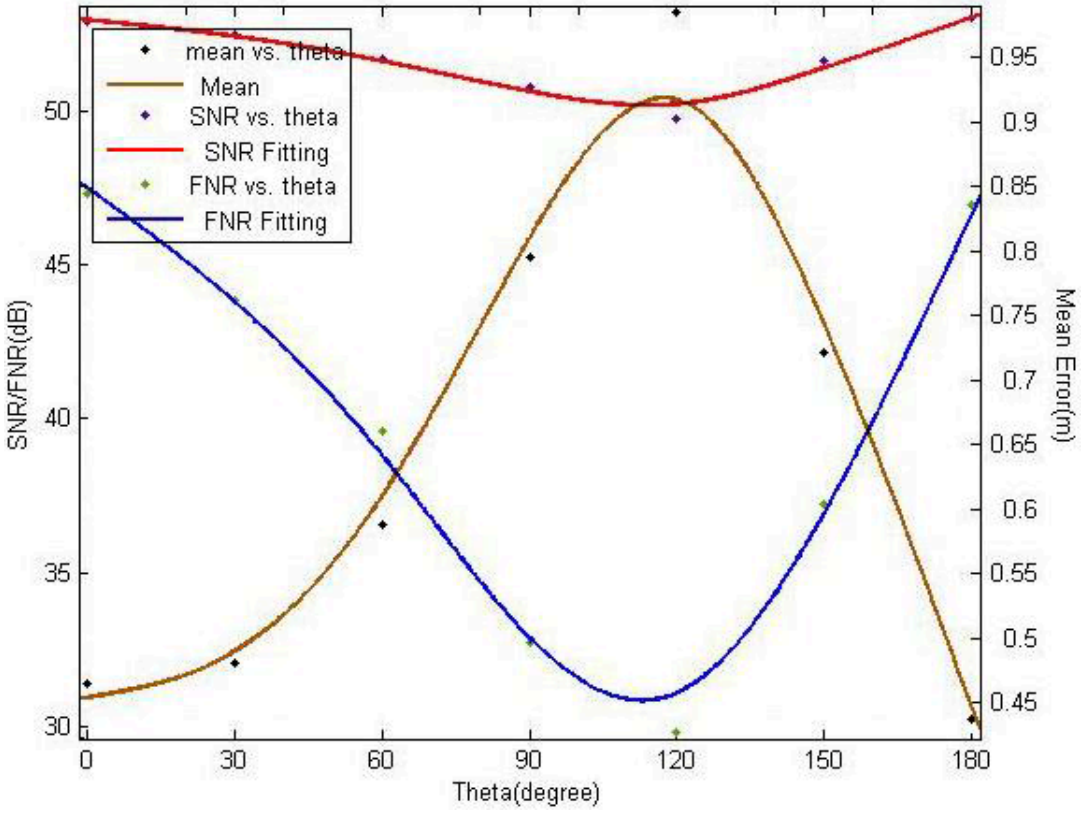

Figure 4.6: Relationship between SNR, FNR and angle . TOA ranging error has been provided as a reference.

4.4 Modeling TOA Ranging Error for Wrist Mouted Sensors

As is mentioned in previous section, the TOA ranging error e can be partitioned into LOS error and DDP error for NLOS scenario, our ranging error model can be defined as:

$$e = \epsilon_M + \delta(P_{NLOS}(\theta) - 1) \times \epsilon_{NLOS} \tag{4.3}$$

where ϵ_M represents the multipath error for LOS scenario, ϵ_{NLOS} represents the error caused by blockage of human body in the NLOS scenario. $\delta(x)$ is an impulse given by (4) and P_{NLOS} is given by (5):

$$\delta = \begin{cases} 1, & x = 0 \\ 0, & x \neq 0 \end{cases} \tag{4.4}$$

$$P_{NLOS}(\theta) = \begin{cases} 1, & \theta \in [0^o, 90^o) \\ 0, & \theta \in [90^o, 180^o] \end{cases} \tag{4.5}$$

4.4.1 Regression Fitting

ϵ_M

The analysis of measurement results proved that the ϵ_M forms a Gaussian distribution. Therefore, it can be modeled as:

$$\epsilon_M = G(\mu_{M,W}, \sigma^2_{M,W}) \tag{4.6}$$

in which the Gaussian random variable has mean $\mu_{M,W}$ and variance $\sigma^2_{M,W}$. Since the geometrical relationship is not involved yet, both $\mu_{M,W}$ and $\sigma^2_{M,W}$ only depend on the system bandwidth.

ϵ_{NLOS}

The total TOA ranging error of NLOS scenario is the combination of both multipath error and DDP error. Due to the fact that the total power (SNR) does not vary a lot between LOS and NLOS scenario, the multipath error for NLOS scenario is almost the same for LOS scenario and we only need to calculate the DDP error. In NLOS scenario, both total TOA ranging error and multipath error follows Gaussian distribution, The DDP error also forms Gaussian distribution and it can be defined as:

$$\epsilon_{NLOS} = G(\mu_{NLOS}, \sigma^2_{NLOS}) \tag{4.7}$$

in which the Gaussian random variable has mean μ_{NLOS} and variance σ^2_{NLOS}. As can be seen from Figure 4.4, in the NLOS part of our measurement result, both mean and variance are symmetric of specific angle θ. The symmetry axis of μ_{NLOS} is around 115^o and symmetry axis of σ^2_{NLOS} is obviously 90^o. Moreover, due to the symmetry feature of NLOS part of figure 4.4, it can be easily modeled by using symmetric functions. Angle β is defined as (8) in order to temporarily represent the biased symmetry axis of μ_{NLOS}.

$$\beta = \theta - 25^o \tag{4.8}$$

For given W and SNR, μ_{NLOS} has the same shape of function $\sin^3(\beta)$ which indicates that linear function of $\sin^3(\beta)$ will be suitable to model it. Also, The shape of σ^2_{NLOS} is too sharp to be modeled by $\sin^3(\beta)$ that we use exponential

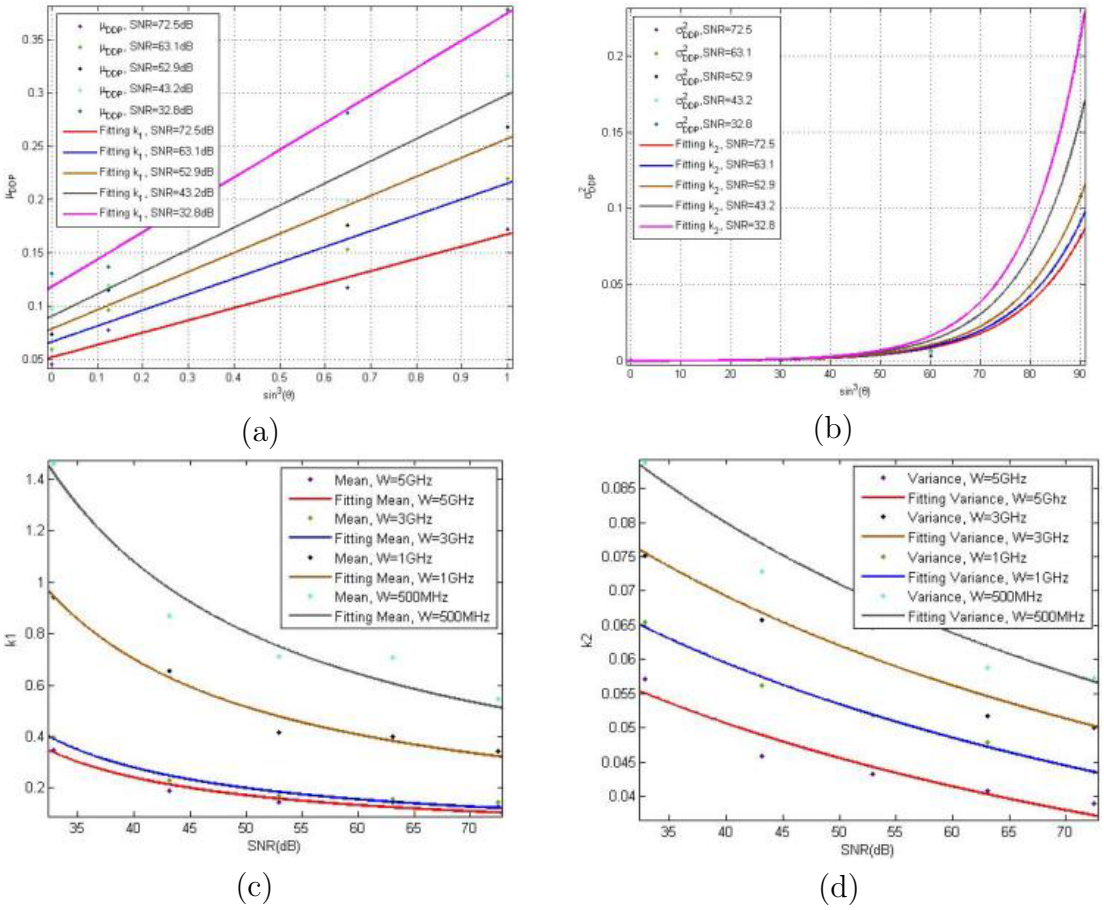

Figure 4.7: Regression fitting results for the TOA ranging error of wrist mounted sensors. (a): μ_{LOS} vs. $\sin^3(\theta)$. (b): σ^2_{LOS} vs. e^{θ}. (c): k_1 vs. SNR_{LOS}. (d): k_2 vs. SNR_{LOS}.

function to model it. The expression for μ_{NLOS} and σ^2_{NLOS} are given as follow:

$$\mu_{NLOS} = k_1 \times \sin^3(\beta) + bias_W \tag{4.9}$$

$$\sigma^2_{NLOS} = 10^{-5} \times e^{k_2\theta} \tag{4.10}$$

where k_1 is the slope of linear function, $bias_W$ is the intercept of linear function and k_2 is the exponent. Figure 4.7 shows the fitting results of μ_{NLOS} vs. β and σ^2_{NLOS} vs. θ with a fixed bandwidth of 5GHz. The fitting result shows that the coefficient k_1 and k_2 increase with the decrease of SNR, indicating that the blockage of human

body increases in low SNR condition. Coefficients k_1 and k_2 are worked out as a rational function of SNR as follow:

$$k_1 = \frac{a_W}{SNR - b_W} \tag{4.11}$$

$$k_2 = \frac{b_W}{SNR - d_W} \tag{4.12}$$

in which a_W, b_W, c_W and d_W are parameters based on system bandwidth W in our model. The curve fitting results for k_1 and k_2 are shown in Figure 4.8 and all these parameters are listed in Table I. According to (4.8), (4.9), (4.10), (4.11) and (4.12), the ϵ_{NLOS} can be modeled as:

$$\epsilon_{NLOS} = G(\mu_{NLOS,W}, \sigma^2_{NLOS,W}) \tag{4.13}$$

where

$$\mu_{NLOS,W} = \frac{a_W}{SNR - b_W} \times \sin^3(\theta - 25^o) + bias_W \tag{4.14}$$

$$\sigma^2_{NLOS,W} = 10^{-5} \times e^{\frac{c_W}{SNR - d_W} \times \theta} \tag{4.15}$$

4.4.2 General Model

Based on all above discussion in this subsection, the general model of TOA ranging error for wrist mounted sensors can be given by:

$$e = \epsilon_M + \delta(P_{NLOS} - 1) \times \epsilon_{NLOS}$$

$$= G(\mu_{M,W}, \sigma^2_{M,W}) + \delta(P_{NLOS} - 1) \times G(\mu_{NLOS,W}, \sigma^2_{NLOS,W}) \tag{4.16}$$

where $\mu_{NLOS,W}$ and $\sigma^2_{NLOS,W}$ are defined in (?) and (?). The values of all the coefficients of the model have been shown in Table I.

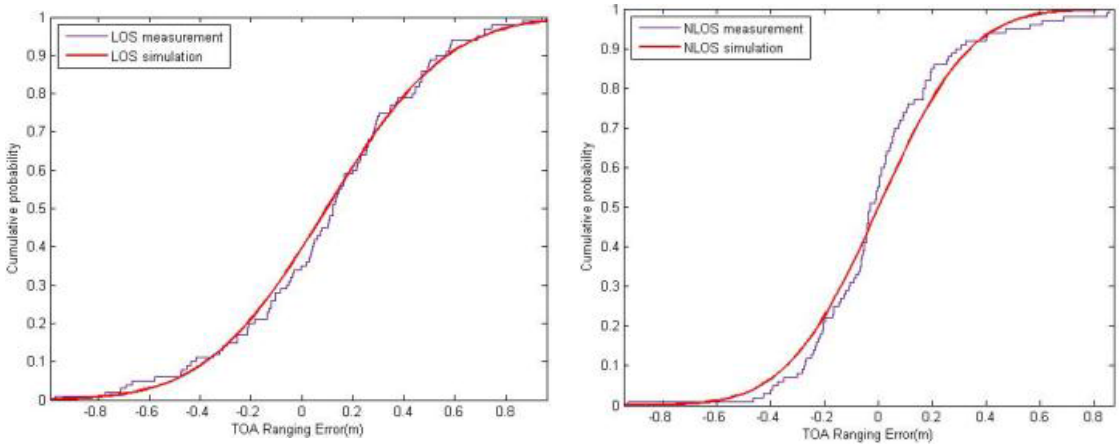

(a) (b)

Figure 4.8: Comparison between empirical measurement result and software simulation result using the model presented above. (a): Comparison of TOA ranging error in LOS scenario. (b): Comparison of TOA ranging error in NLOS scenario, $Case = \{0^o, 62.0dB, 3GHz\}$.

4.4.3 Model Validation

Comparison between simulated result from our model and empirical measurement data has been made in the purpose of model validation. CDF of ranging error for both LOS and NLOS scenario are presented in Figure 4.9, in which we take W=3GHz, SNR=63.1dB case as an example. The validation result on the left hand figure shows that for LOS scenario, our model perfectly matches the measurement data while for NLOS scenario, close agreement between simulation and measurement result still exists.

Table 4.1: Coefficients for the TOA ranging error model for wrist mounted sensors.

W(GHz)	$\mu_{M,W}$(m)	$\sigma^2_{M,W}$(m)	a_W	b_W	$\text{SNR}_{Thre,W}$(dB)
5	0.010	0.005	5.10	5.49	30.4
3	0.009	0.001	3.98	6.69	30.4
1	0.072	0.058	6.21	11.76	29.0
0.5	0.138	0.143	14.69	10.62	27.5

4.5 Comparison Between Chest Mounted Case and Wrist Mounted Case

In this subsession, we provided explanation for the difference between this human wrist model and the human chest model in our previous work.

The LOS part of human chest model in previous chapter is modeled in the same way as our wrist model in this chapter. However, obvious differences can be found in the NLOS scenario. In chest model, the NLOS scenario is modeled as:

$$\epsilon_{NLOS} = G(\mu_{NLOS,W}, \sigma^2_{NLOS,W}) \tag{4.17}$$

where

$$\mu_{NLOS,W} = \frac{a_W}{\text{SNR}_{LOS} - \text{SNR}_{Thrd,W}} \times \cos^3(\theta) \tag{4.18}$$

$$\sigma^2_{NLOS,W} = \frac{b_W}{\text{SNR}_{LOS} - \text{SNR}_{Thrd,W}} \times \cos^3(\theta) \tag{4.19}$$

By comparing (4.14) and (4.18), its easy to notice that the wrist has a 25^o bias on the symmetry axis and an extra intercept on the expression of mean value for all bandwidth options. To explain the bias on symmetry axis, sectional view of human body is provided in Figure 4.9 with two major creeping waves around human body in green and pink. From Figure 4.9 we see that, different from human

chest scenario, when the antenna is attached to human wrist, the sectional view is no longer symmetric. The maximum mean error is supposed to appear at the time when two major waves travel along the same distance. However, at 90^o, the pink wave travels a lot more than the green one. Due to the fact that the midpoint is located at approximately 115^o, the maximum mean error appears at that angle. Apart from that, the intercept on mean value may come from the undesirable propagation channel between human wrist and human trunk.

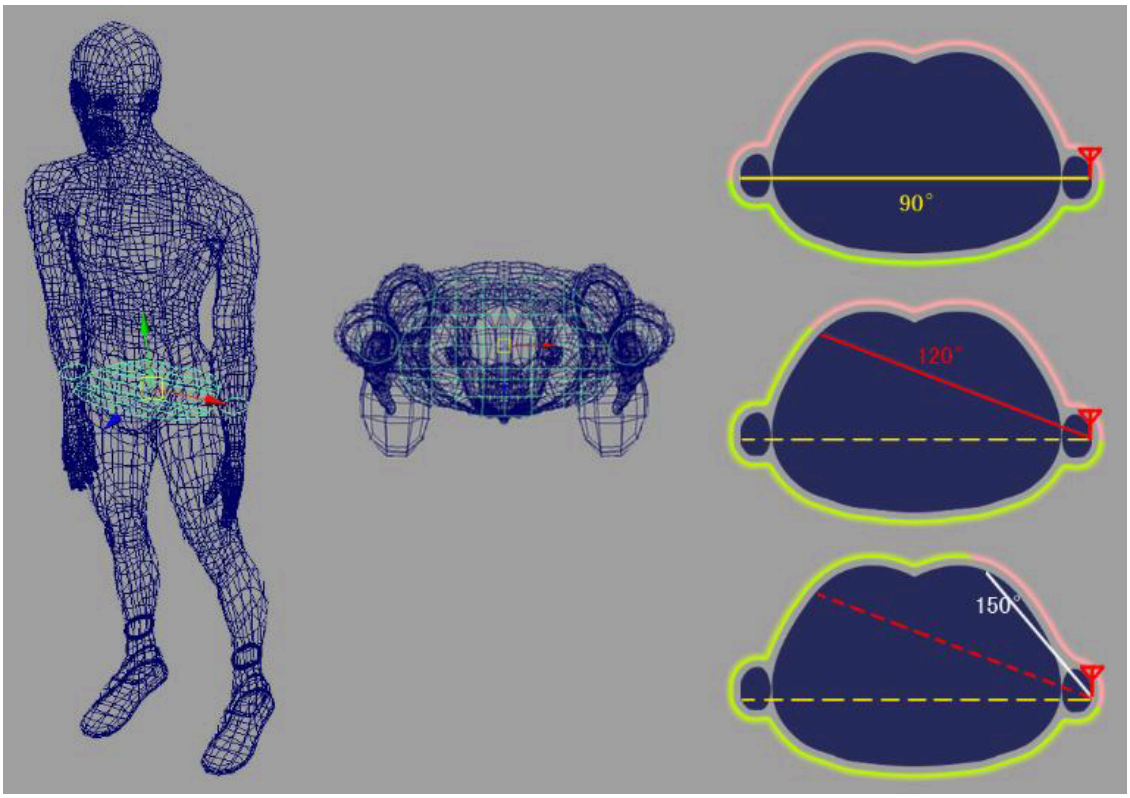

Figure 4.9: Creeping wave phenomenon around the surface of human body for the wrist mounted sensors.

As for the different expression pattern of variance, at 30^o and 150^o there is only a mere part of human body blocking the direct line of sight between TX and RX, resulting in a relatively small variance and the change of variance is too sharp to be modeled by $\sin^3(\beta)$, resulting in an exponential function.

4.6 Summary

In this chapter, measurement has been conducted focusing on ranging error of TOA based indoor localization when human body is regarded as a blockage of direct line of sight. Analysis on effects of geographical relationship, bandwidth and power has been presented and accurate statistical model of TOA ranging error has been built. We attach the receiver antenna to human wrist and obtained distinct model from the human chest model in our previous work. Empirical measurement result shows that both multipath error in LOS scenario and DDP error in NLOS scenario can be modeled as Gaussian variable and the difference between wrist model and chest model can be explained from the perspective of creeping wave along human body.

Chapter 5

Empirical Near Body Channel Model for Effects of Human Body

5.1 Introduction

The mergence of wireless body area networks (WBAN) and wireless local area networks (WLAN) are finding an increasing number of applications in indoor environment such as health monitoring, indoor human tracking and etc. and such rapid expansion results in significant advances in the development of wireless access and localization. Since the ultimate performance of these applications is limited by the wireless channel they operate in, researches on propagation characteristics received much attention in the recent years [DCM02]. Among the available spectrum resources, ultra-wideband (UWB) is one of the most promising candidate for these indoor applications due to its fading tolerance, lower interference and easier penetration on the communication aspect as well as the high accuracy property on the localization aspect.

A number of traditional statistical UWB channel models for indoor environ-

ment have been posted in the literature. [DCM02] proposed a wide band channel model which is later on adopted by IEEE 802.15.4a for low frequency UWB system evaluation. [AMp03] is adopted by the IEEE 802.15.3a group as the standard UWB channel model for frequency ranging from 3GHz to 10GHz. In the latest IEEE 802.15.6 standard for body area networks, UWB models are also developed for the channel from body surface to body surface (CM3) and from body surface to external access point (CM4) [tg610]. Such statistical models are easy-to-use and computationally efficient in general, but they suffer the lack of accuracy due to the fact that statistical models are derived from extensive measurement results which are not specific to the intended deployment environment [HAP97].

To avoid the costly and time consuming field measurement, the most popular method to come up with the site-specific propagation characteristics is ray-tracing [JHW12]. Ray-tracing technique is an approach that can obtain channel characteristic by identifying the contributions of individual multipath component and calculating their composition at the receiver. Since each individual multipath component is described in terms of rays, optical effects such as absorption, reflection and diffraction of surrounding walls and stuff that make up the indoor environment can be taken into account. As for BAN applications, human body itself also has a strong influence on the waveform propagation and it can be regarded as a special and complex obstacle to the passing rays. However, no ray-tracing model considering human body can be found in the open literature until now.

Related researches reported that the over 80 dB penetration loss eliminates the direct path that penetrate the human body and the radio frequency (RF) signal get scattered on the surface of human body and travels in the pattern of creeping wave [JHP12b] [AFe05]. As is mentioned before, the IEEE 802.15.6 group developed pathloss model for CM3 and CM4. However, these given channel models are not

adequate to design ray-tracing model considering human body for the following reasons: 1) When passing the human body, the behavior of creeping wave should be modeled as a function of both distance and incidence angle. 2) The behavior of creeping wave should be modeled as the joint propagation characteristics of CM3 and CM4. 3) Apart from the total pathloss, power of each individual path is also critical in designing ray-tracing technology.

In this chapter, measurements have been conducted inside an anechoic chamber with the transmitter (Tx) mounted to the chest of human body and receiver (Rx) located in the surrounding area with different distance to Tx and different incidence angle. Based on the empirical measurement result, the pathloss of the first path has been modeled to be partitioned into two sections by the break point. The break point is modeled as a function of incidence angle and the first section of the model is observed to have a negative pathloss. Time-of-arrival (TOA) of the first path has been modeled as a two-section model as well with the same break point used in the pathloss model of the first path. The total pathloss has very similar trend with the pathloss of the first path so that they are modeled by the same equation with different coefficients. The empirical model presented in this chapter illustrates the behavior of RF waveform when passing the human body and can be regarded as the theoretical basis of the further development of the ray-tracing technique with human body taken into consideration.

5.2 Measurement Setup

The empirical measurements are performed in the frequency band ranging from 3GHz to 8GHz in an anechoic chamber. The methodology of data collection will be discussed in detail in this section.

5.2.1 Measurement Settings

The measurement system employed in this chapter consists of a vector network analyzer (VNA, Agilent E8363), a pair of low loss cable, a 30dB power amplifier and a pair of small size UWB patch antenna (Skycross SMT-3TO10M). The power amplifier is employed to guarantee the peak detection at the Rx side due to the huge pathloss of the near body channel. A medium size male remaining standing posture is selected as the objective of the measurement. The Tx atenna has been attach to the middle of the human chest at the height of 1.29m while the Rx antenna is tied to a tripod of the same height. Since the antenna-body interaction is an integral part of the overall propagation characteristic, the influence of antenna has been included as a part of our model. Parameters used in VNA calibration are listed in Table 5.1 and system components are connected as is depicted in Figure 5.2.1.

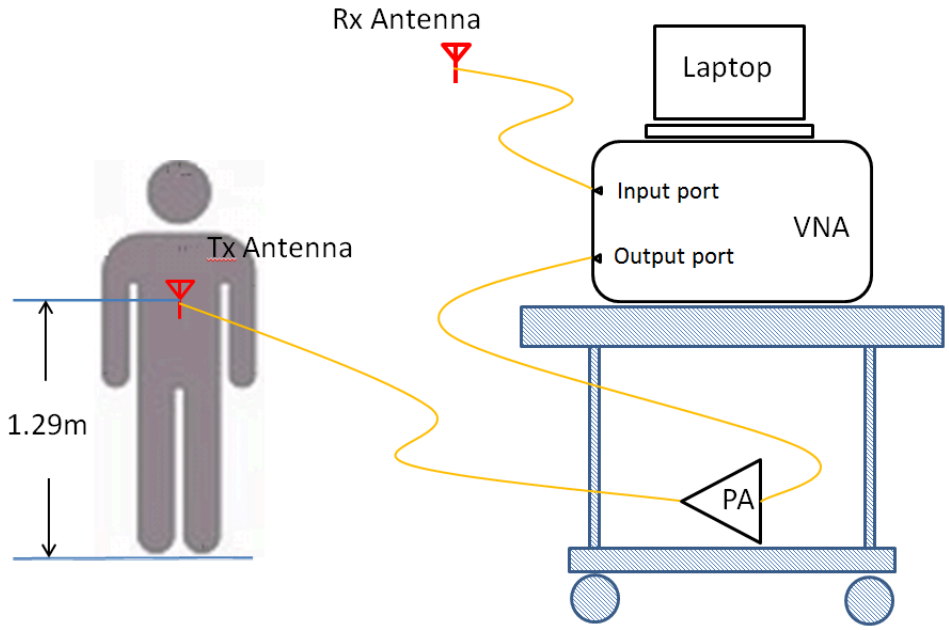

Figure 5.1: Sketch of the UWB measurement system.

The S parameter S_{21}, which is also known as the channel transfer function has

Table 5.1: Specification of VNA and antenna for the measurement system

Parameters	Values
VNA	Agilent E8363
Frequency Range	3-8 GHz
Sample point number	1601
Calibration	Responese
Transmit power (P_{Tx})	0 dBm
IF Bandwidth	3 KHz
Antenna	Skycross SMT-3TO10M

been measured by the VNA in frequency domain. The recorded spectrum profile $Y(\omega)$ is given by:

$$Y(\omega) = H(\omega)X(\omega) + N(\omega) \tag{5.1}$$

where $H(\omega)$ represents the channel impulse response and $N(\omega)$ represents the addictive white Gaussian noise (AWGN), respectively [XCe11]. A symmetric hamming window has been applied to the frequency domain at the cost of time resolution in order to limit the sidelobe and enable detection of more multipath component. The hamming window is given by:

$$\omega(n) = \begin{cases} 0.54 - 0.46\cos(\frac{2\pi n}{N}), & 0 \leq n \leq N \\ 0, & \text{otherwise} \end{cases} \tag{5.2}$$

The frequency domain profile is transferred to time domain by a base band complex inverse fast Fourier transform (IFFT). Typical recorded time domain channel profile has been shown in Figure 5.2.1 in which proper threshold has been established to detect the first path, thus determine the first path pathloss and first path TOA.

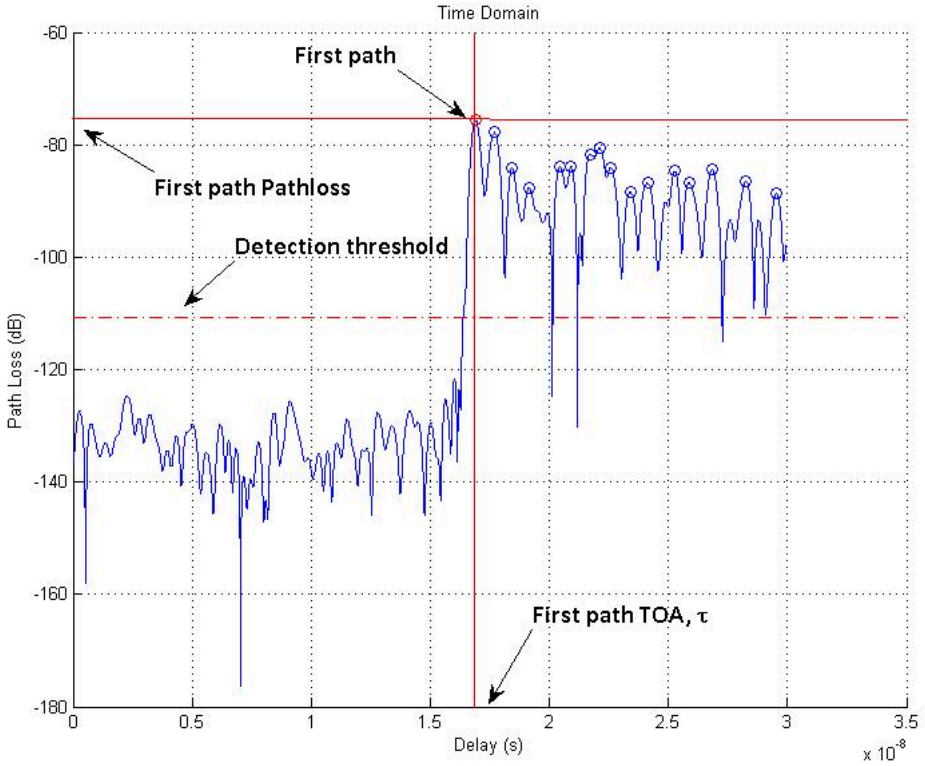

Figure 5.2: Sample time domain channel profile with detection threshold, power of the first path and Time-of-arrival of the first path.

5.2.2 Measurement Scenario

From the perspective of scenario-based approach, a measurement case set denoted by:

$$Case = \{\theta, d\}$$

is composed of a subset θ which is the incidence angle of rays and subset d which is the distance between Tx and Rx. A specific case of our measurement can be $Case = \{30^o, 0.6m\}$. Over 300 snapshots are obtained in each case to guarantee the validity of the near body model.

Incidence Angle θ

The Incidence angle is defined as the horizontal angle between human facing direction and the direction of Tx-Rx. Fig. 3 shows the torso section extracted from 3D scan of our measurement objective. It is at the same height of Tx antenna which is 1.29m. The section is then attached to a protractor plane and a 30^o sample incidence angle can be seen clearly. The measurements are performed every 30^o so that the subset θ is given by:

$$\theta = \{0^o, 30^o, 60^o, 90^o, 120^o, 150^o, 180^o\}$$

The measurement cases are also partitioned into line-of-sight (LOS) and non-line-of-sight (NLOS) scenarios by whether the human body is blocking direct line between Tx and Rx. To help classify these two scenarios, we define the relationship between incidence angle θ and physical scenario S as:

$$S = \begin{cases} NLOS, & \theta \in [0^o, 90^o] \\ LOS, & \theta \in (90^o, 180^o] \end{cases} \tag{5.3}$$

Tx-Rx distance d

Since the RF waveform travels as creeping wave along the surface of human body, one possible approach is to define d as the actual travel distance which is the combination of both on-body creeping distance and off-body propagation distance. However, to facilitate the modeling process, we define the Tx-Rx distance d as the straight-line distance between Tx and Rx.

The definition of d can be also seen in Fig. 3. Throughout the measurements,

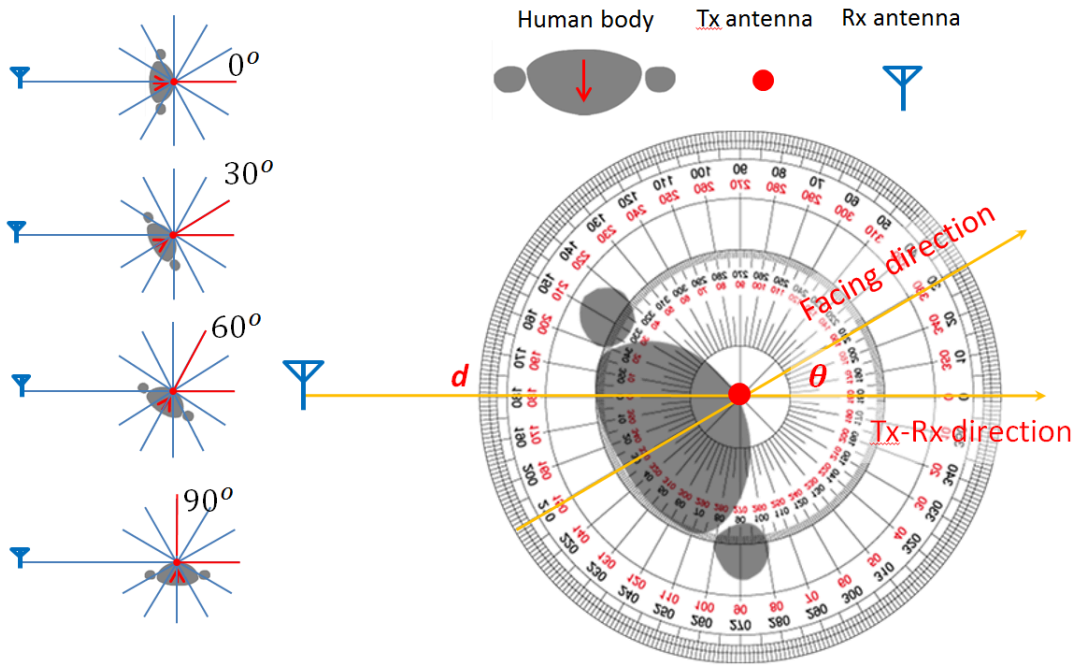

Figure 5.3: Definition of incidence angle θ and Tx-Rx distance d.

both the locations of Tx antenna and the Tx-Rx direction are fixed and the variation of incidence angle θ is achieved by changing the standing position and facing direction of the objective. For each incidence angle θ, the Rx antenna has been initially located at the minimum possible distance $d_{0,\theta}$ and then moved away from human body for every 10cm along the Tx-Rx direction. The maximum distance between Tx and Rx is limited within 1.1m so that the distance subset can be given by:

$$d = \{d_{0,\theta}, 30\text{cm}, 40\text{cm}, 50\text{cm}, ..., 100\text{cm}, 110\text{cm}\}$$

In LOS scenario and the 90^o case of NLOS scenario, existence of human body does not hinder the Rx antenna set up so that we let $d_{0,\theta} = \{10cm, 20cm\}$. In rest of the NLOS scenario, minimum possible initial distance $d_{0,\theta}$ is the intersection point of body surface and Tx-Rx direction. Since it depends on the size and shape of human body involved in the measurement, we calculated the $d_{0,\theta}$ on the torso

section and listed the values of $d_{0,\theta}$ in table II.

5.3 Empirical Near Body Model

In this section, we first discuss the propagation characteristic of the near body UWB channel separately in LOS and NLOS scenario and then provide an general model for both scenarios.

5.3.1 First Path Pathloss

LOS scenario

Empirical measurement result shows that, in LOS scenario, the first path pathloss is independent to the incidence angle θ so that we calculate the mean and variance of measurement results for each Tx-Rx distance d in the subset and plot them in Fig. 4. As can be seen from the linear regression fitting result in Fig. 4, the first path pathloss $P_{first}(d)$ can be modeled as a linear function of d:

$$P_{first}(d) = L_{0,\mathrm{LOS}} + 10\alpha_{1,\mathrm{LOS}} \log_{10}(d) + S_{\mathrm{LOS}} \tag{5.4}$$

where d is the Tx-Rx distance defined in previous section, $L_{0,\mathrm{LOS}}$ denotes to the pathloss at reference distance of 0 mm, $\alpha_{1,\mathrm{LOS}}$ is the pathloss exponent representing the fading rate and $S_{\mathrm{LOS}} \sim (0, \sigma^2)$ denotes to the fluctuation term of the first path pathloss in LOS scenario.

NLOS scenario

The measurement results of 90^o case in NLOS scenario has been also depicted in Fig. 4. In that case, the first path pathloss can be also modeled as a linear function

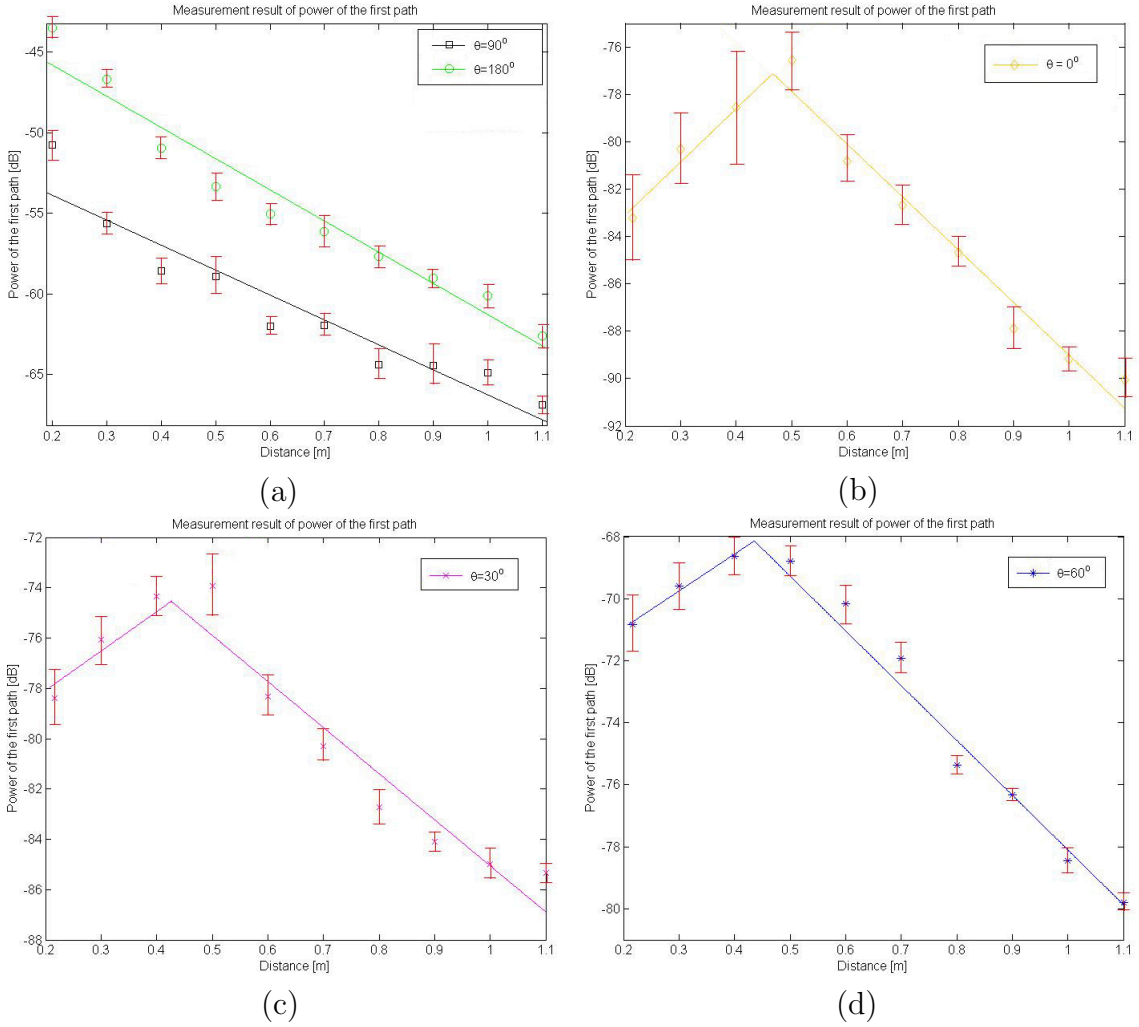

Figure 5.4: First path pathloss in NLOS scenario. (a): LOS scenario and $\theta = 90^o$ for NLOS scenario. (b): $\theta = 0^o$. (c): $\theta = 30^o$. (d): $\theta = 60^o$.

of d with very similar fading rate ($\alpha_{1,90^o}$) but different pathloss at reference distance ($L_{0,90^o}$) compared with LOS scenario. The model of 90^o case in NLOS scenario is given by:

$$P_{first}(d) = L_{0,90^o} + 10\alpha_{1,90^o} \log_{10}(d) + S_{90^o} \tag{5.5}$$

An approximately 8dB bias between $L_{0,90^o}$ and $L_{0,\mathrm{LOS}}$ can be seen from Fig. 4, which is caused by the effect of human body in 90^o case.

As for the rest of cases in NLOS scenario, the signal strength of detected first

path has been shown in Fig 5.(a) (b) and (c). Three observation can be brought about from the empirical measurement results: 1) Pathloss of the first path has been partitioned into two sections by a distance break point. The break point is between 0.4 and 0.5m; 2) In the first section, a negative increase on first path pathloss can be observed while in the second section, it becomes positive increase; 3) The range of fluctuation of first path pathloss in the first section is much larger than that of the second section.

Reasonable explaination can be made for the above mentioned observations. Fig. 6 sketched the near body propagation route that RF signal travels along. Waveforms start from the Tx antenna, creep to the other side of human body along the body surface and then get scattered at specific point. The the scatter point serve as another antenna and the scattered waveforms continue propagating in free space and finally reach the Rx antenna. As a result, with the increment of Tx-Rx distance, the creeping distance decreases while the free space propagation distance increases. According to the distance based UWB on body model proposed in [AFe05], the on body signals get much more attenuation per unit distance compared with the signal in free space, so that creeping phenomenon is dominating the pathloss of first section while the free space propagation masters the pathloss of second section. Based on the analysis, we define the first section as on-body section and second section as off-body section. The alternation of effects of two phenomenons takes place at the break point and the larger fluctuation of on-body section also has an agreement with [AFe05].

Since each of the two sections has a linear trend individually, the overall pathloss

Table 5.2: Coefficients for the near body UWB model with perspective of the first path pathloss.

θ	d_0	d_{bp}	First path pathloss				
			$L_{0,\theta}$	$\alpha_{1,\theta}$	$\alpha_{2,\theta}$	$S_{\text{on-body},\theta}$	$S_{\text{off-body},\theta}$
0	0.2134	0.497	71.34	-1.757	4.022	3.1750	0.9814
30	0.1927	0.463	69.74	-1.259	3.167	2.3146	0.8947
60	0.2164	0.411	65.32	-0.926	2.194	1.2615	0.5250
90	10, 20	inf	65.75	2.081	NA	0.4742	NA
LOS	10, 20	inf	60.46	2.485	NA	0.3934	NA

of the first path can be modeled as:

$$P_{first}(d) = L_{0,\theta} + \begin{cases} 10\alpha_{1,\theta}\log_{10}(d) + S_{\text{on-body},\theta}, & d \le d_{bp,\theta} \\ 10\alpha_{1,\theta}\log_{10}(d_{bp,\theta}) & \\ \quad +10\alpha_{2,\theta}\log_{10}(d/d_{bp,\theta}) + S_{\text{off-body},\theta}, & d > d_{bp,\theta} \end{cases} \tag{5.6}$$

where $d_{bp,\theta}$ is the distance break point, $\alpha_{1,\theta}$ and $\alpha_{2,\theta}$ denote to the pathloss exponent that determine the fading rate in each section, $S_{\text{on-body}}$ and $S_{\text{off-body}}$ are fluctuation terms, and $L_{0,\theta}$ denotes to pathloss at the reference distance of 0mm again. All of the coefficients in this model are related to incidence angle θ.

General model

When $d \le d_{bp}$, the pattern of equation (6) is identical to equation (4) and (5) so that given infinity d_{bp} in LOS scenario and 90^o case of NLOS scenario, equation (6) can be used to uniformly represent the first path pathloss. Values of all these coefficients are listed in table II.

5.3.2 First Path Time-of-Arrival

Another important aspect in designing the ray-tracing technology considering the effects of human body is the arrival time of first path. That aspect is especially important for TOA based localization applications. To get a better understanding on the effects of human body on first path TOA, we plot the empirical result for all measurement cases in Fig. 7.

LOS scenario

Figure 5.3.3 shows that, in LOS scenario, the first path TOA is a linear function of Tx-Rx distance d which can be modeled as

$$\tau(d) = \gamma_{\text{LOS}}(d) + \delta_{\text{LOS}} \tag{5.7}$$

where $\tau(d)$ represents the first path TOA, γ_{LOS} denotes to the velocity of first path in LOS scenario and δ_{LOS} represents the delay caused by human body. By comparing the empirical measurement results with the free space propagation characteristics, a negligible 0.065ns bias can be observed in LOS scenario.

NLOS scenario

Same situation happens in the 90^o case in NLOS scenario. There is no creeping distance in that case so that the first path TOA is still linear. However, the bias caused by human body goes up to 0.2ns and the first path TOA for 90^o case is given by:

$$\tau(d) = \gamma_{90^o}(d) + \delta_{90^o} \tag{5.8}$$

where γ_{90^o} denotes to the velocity of 90^o case in NLOS scenario and δ_{90^o} represents the bias with free space propagation.

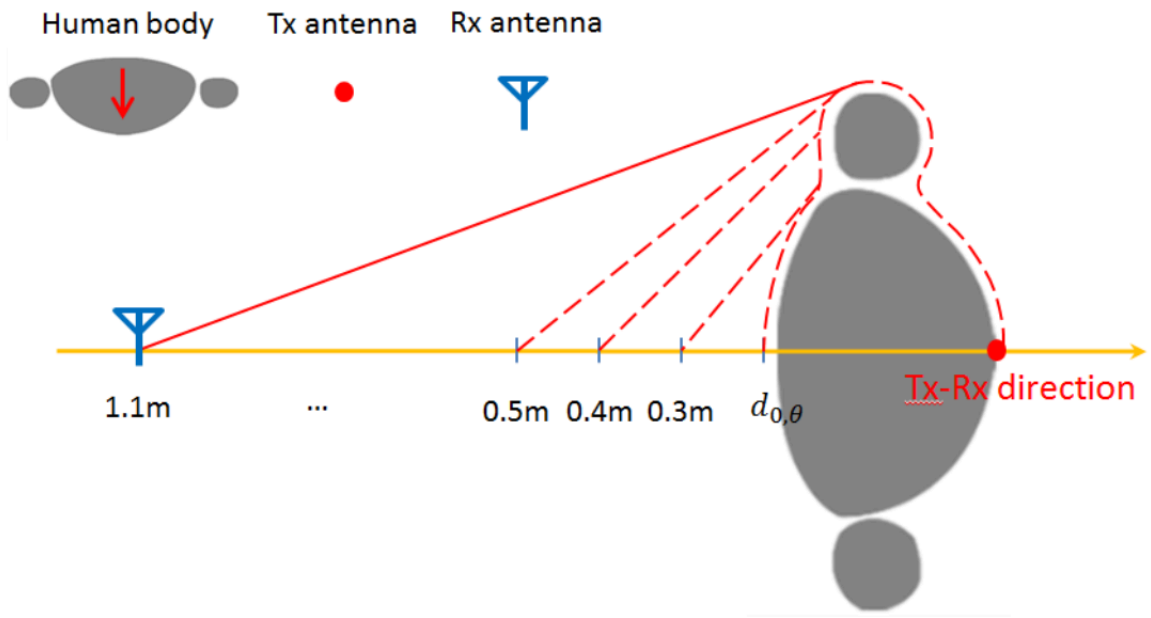

Figure 5.5: Sketch of the propagation route from Tx to Rx including both creeping distance and free space propagation distance.

As for $0^o, 30^o$ and 60^o cases in the NLOS scenario, the model of first path TOA can be also partitioned into two sections in the same way as the first path pathloss model. Our empirical measurement results in Fig.7 shows that the break points for each incidence angle θ is also identical to the first path pathloss model. In the on-body section, the first path TOA has a smaller velocity compared with free space velocity because the the actual creeping distance for the on-body section is longer than the straight-line distance employed in the model. However, in off-body section, the velocity of waveform is almost the same as free space propagation when the actual propagation distance becomes very close to the straight-line distance. One thing also worth mentioning is that in the angle based on body UWB model proposed by [JCP12], first path TOA is modeled as $\tau(\theta) = \frac{\theta\pi}{360} + \Delta t$, indicating an approximately 5ns delay for every 30^o difference in the incidence angle. Fig. 7 shows that in the on-body section, the bias between two neighboring measurement

cases has a close agreement with the model in [JCP12] while in the off-body section, the bias is smaller. Such agreement also proves the validity of the physical process described in Fig. 6.

Based on above analysis, the first path TOA in these cases can be modeled as:

$$\tau(d) = \begin{cases} \gamma_{\text{on-body},\theta}(d) + \delta_{\text{on-body},\theta}, & d \leq d_{bp,\theta} \\ \gamma_{\text{off-body},\theta}(d) + \delta_{\text{off-body},\theta}, & d > d_{bp,\theta} \end{cases} \tag{5.9}$$

where the $\gamma_{\text{on-body},\theta}$ and $\gamma_{\text{off-body},\theta}$ represents the velocity of waveform for on-body and off-body section and $\delta_{\text{on-body}}$ and $\delta_{\text{off-body}}$ represents the time delay caused by human body.

General model

Similar with the the model for first path pathloss, the first path TOA model for LOS scenario and 90^o case in NLOS scenario can be merged into the a general model due to the fact that equation (7) (8) and (9) share the same pattern. The general model is given by:

$$\tau(d) = \begin{cases} \gamma_{\text{off-body},\theta}(d) + \delta_{\text{off-body},\theta}, & \theta \in (90^o, 180^o] \\ \gamma_{\text{on-body},\theta}(d) + \delta_{\text{on-body},\theta}, & \theta \in [0^o, 90^o], d \leq d_{bp,\theta} \\ \gamma_{\text{off-body},\theta}(d) + \delta_{\text{off-body},\theta}, & \theta \in [0^o, 90^o], d > d_{bp,\theta} \end{cases} \tag{5.10}$$

where $\tau(d)$ represents the first path TOA, d_{bp} denotes to the distance break point, $\gamma_{\text{on-body},\theta}$ and $\gamma_{\text{off-body},\theta}$ represents the velocity of RF signal and $\delta_{\text{on-body},\theta}$ and $\delta_{\text{off-body},\theta}$ represents the bias from free space propagation. All these coefficients are related to the incidence angle θ and for 90^o case in NLOS scenario, the d_{bp} is set to infinity.

Table 5.3: Coefficients for the near body UWB model in perspective of Time-of-arrival of the first path.

θ	d_0	d_{bp}	First path TOA			
			$\gamma_{\text{on-body},\theta}$	$\gamma_{\text{off-body},\theta}$	$\delta_{\text{on-body},\theta}$	$\delta_{\text{off-body},\theta}$
0	0.2134	0.497	0.656	3.345	1.225	2.521
30	0.1927	0.463	0.842	3.331	0.994	2.042
60	0.2164	0.411	0.997	3.314	0.419	1.532
90	10, 20	inf	NA	3.341	NA	0.204
LOS	10, 20	inf	NA	3.347	NA	0.065

5.3.3 Total Pathloss

The total pathloss is obtained from an approach that is different from the first path pathloss and first path TOA. Since the total pathloss is the integration of pathloss on the whole frequency band, instead of recording the time domain channel profile, we abtained the total path according to the following equation:

$$P_{total}(d) = -20\log_{10}(\frac{1}{N_s}\frac{1}{N_f}\sum_{i=1}^{N_s}\sum_{n=1}^{N_f}|H_i^p(n)|) \tag{5.11}$$

where $P_{total}(d)$ is the total pathloss at distance d, N_s is the number of snapshots which is 300 in this chapter, N_f is the number of frequency sample points in each snapshot which is 1601 and $H_i^p(n)$ is the S_{21} reading at each sample point from the VNA.

Sample measurement results of the total pathloss has been depicted in Fig. 8 for which the incidence angle $\theta = 0^o$. The distance break point is still identical to the first path pathloss model. From the figure we see that for each distance, although most of the energy condensed on the first path, the total power at the receiver side is still higher than the power of the first path. In both on-body and off-body sections, we also observed more gentle change on the total power compared with the power of

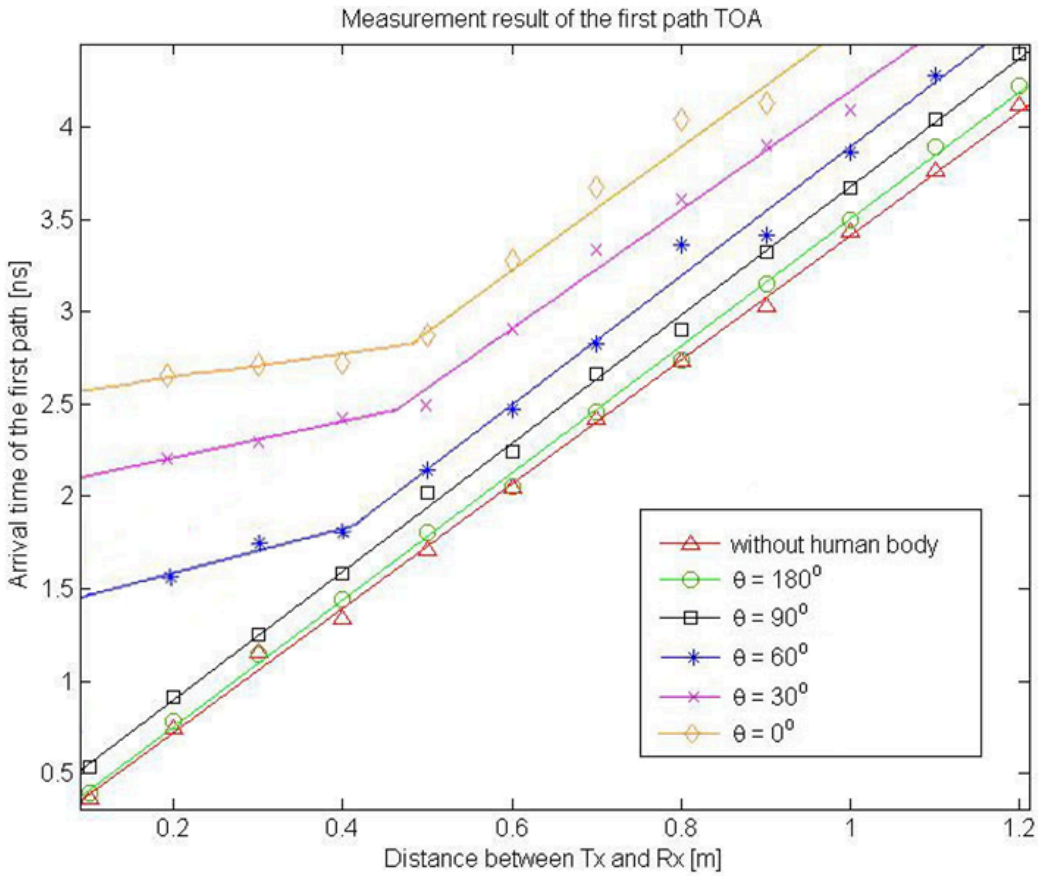

Figure 5.6: First path TOA in all measurement cases where LOS scenario and $\theta = 90^o$ are linear while other rest of NLOS scenarios are two-sectioned.

first path and minimum bias between total power and power of the first path occurs at the break point.

According to the similar approach in deriving the first path pathloss model, the total pathloss of near body UWB channel can be given as:

$$P_{total}(d) = L_{0,\theta} + \begin{cases} 10\beta_{1,\theta}\log_{10}(d) + S_{\text{on-body},\theta}, & d \le d_{bp,\theta} \\ 10\beta_{1,\theta}\log_{10}(d_{bp,\theta}) & \\ \quad +10\beta_{2,\theta}\log_{10}(d/d_{bp,\theta}) + S_{\text{off-body},\theta}, & d > d_{bp,\theta} \end{cases} \tag{5.12}$$

where $P_{total}(d)$ represents the total pathloss for near body UWB channel, $d_{bp,\theta}$ is the

same distance break point as previous models, $\beta_{1,\theta}$ and $\beta_{2,\theta}$ denotes to the fading rate and $S_{\text{on-body},\theta}$ and $S_{\text{off-body},\theta}$ is the fluctuation term. $d_{bp,\theta}$ for all LOS scenario and the 90^o case in NLOS scenario is infinity and all these coefficients are listed in table II.

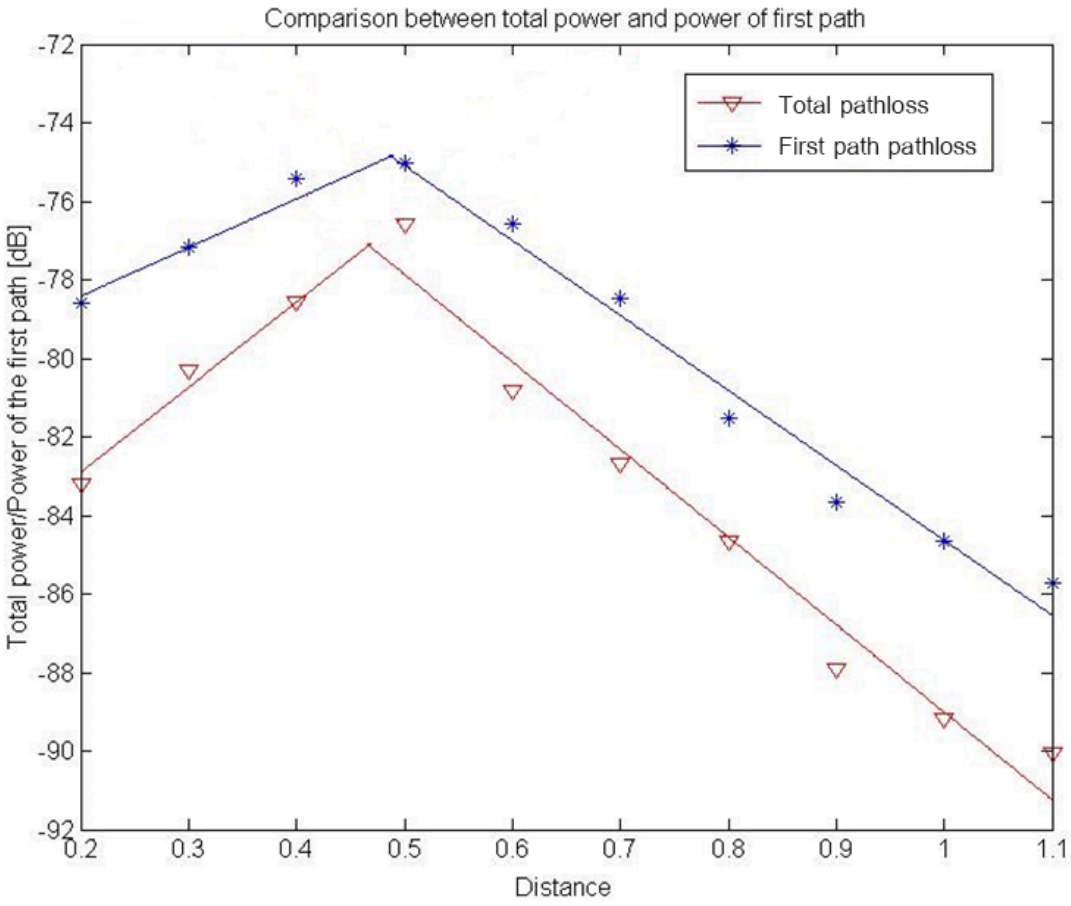

Figure 5.7: Total pathloss for the UWB near body channel in the measurement case of $\theta = 0^o$.

5.4 Summary

In this Chapter, a near body UWB channel model has been built based on empirical measurement conducted inside an anechoic chamber. The frequency range of the

Table 5.4: Coefficients for the near body UWB model in perspective of total pathloss of of the channel.

θ	d_0	d_{bp}	Total pathloss				
			$L_{0,\theta}$	$\beta_{\text{on-body},\theta}$	$\beta_{\text{off-body},\theta}$	$S_{\text{on-body},\theta}$	$S_{\text{off-body},\theta}$
0	0.2134	0.497	72.03	-0.943	3.237	3.0252	0.8751
30	0.1927	0.463	70.43	-0.723	1.902	2.1902	0.8324
60	0.2164	0.411	65.96	-0.598	1.798	1.2957	0.6553
90	10, 20	inf	64.87	2.125	NA	0.4551	NA
LOS	10, 20	inf	60.02	2.329	NA	0.3356	NA

near body model is from 3GHz to 8GHz, covering most of the UWB band. The near body model concentrates on three critical aspects of propagation characteristics which are first path pathloss, first path TOA and total pathloss. All these aspects have been partitioned into on-body section and off-body section based on whether the creeping phenomenon or the free space propagation is dominating the characteristics of the channel. The purpose of creating the near body channel model is to enable the development of ray-tracing technology that can take the effect of human body into consideration. Such model will further facilitate the advancement of wireless access and localization due to the fact that cells are becoming smaller and BAN will take over the attention of both academic and industry at last.

For future work, we plan to repeat all the measurements in finite difference time domain (FDTD) software simulation to validate the near body model. Also, except for the human chest, on body sensors are often located on human wrist, waist, ankle or inside trouser pocket. According to the analysis in this chapter, we infer that the near body model also depends on the location of on body sensor so that related research is still in demand. The next step is to merge the near body model into the channel model between body surface and external access point and we may try to update our ray-tracing software by designing human body module for it.

Chapter 6

Conclusion and Future Work

In this master thesis, we first investigated the effects of human body orientation and sensor locations on TOA ranging error. We introduce a TOA ranging error model for body mounted sensors based on the measurements in a typical office building. This model separates the ranging error into multipath error and NLOS error, which is caused by the penetration loss of the human body and the creeping wave around human body. Both multipath error and NLOS error are modeled as a Gaussian variable. The distribution of multipath error is related to bandwidth of the system while the distribution of NLOS error is related to the angle between the human facing direction and the direction of TX-RX, SNR and bandwidth of the system, which clearly shows the effects of human body on TOA ranging. The comparison between the empirical ranging error and simulated ranging error depicts close agreement, proving the validity of the TOA ranging error for body mounted sensors.

After that, we built a near body UWB channel model based on empirical measurement conducted inside an anechoic chamber. The frequency range of the near body model is from 3GHz to 8GHz, covering most of the UWB band. The near body

model concentrates on three critical aspects of propagation characteristics which are first path pathloss, first path TOA and total pathloss. All these aspects have been partitioned into on-body section and off-body section based on whether the creeping phenomenon or the free space propagation is dominating the characteristics of the channel. The purpose of creating the near body channel model is to enable the development of ray-tracing technology that can take the effect of human body into consideration. Such model will further facilitate the advancement of wireless access and localization due to the fact that cells are becoming smaller and BAN will take over the attention of both academic and industry at last.

The contribution of this thesis is three-folded: 1) we analyzed the effect of human body orientations and sensor locations on the effects of TOA ranging error. 2) We proposed an TOA ranging error model based on SNR, system bandwidth and human body orientation. Such analysis to a great degree facilitated the performance evaluation and algorithm design of TOA based indoor localization system. 3) We investigated the propagation characteristic of the UWB near body model. The channel model can be used in developing ray-tracing technology that considers the effect of human bod, thus optimizes the localization accuracy.

Appendix A

Appendix

A.1 Sample matlab code used in processing channel profile.

```
OrgBand=3e9;   %Orignal Bandwidth from 3Ghz to 8Ghz
B_start=3e9; %Low frequency of select Bandwidth
Band=3e9;      %Slected Bandwidth
noi = -50;     %noise threshold
side =-30;
tstart=0e-9;
if Band>0.3e9
    tstop = 30e-9;
else
    tstop = 100e-9;
end
P_num=fix((Band/OrgBand)*1601);
if B_start~=3e9
```

```
    P_start=fix(((B_start-3e9)/OrgBand)*1601);
else
    P_start=1;
end
P_stop=P_start+P_num-1;
WaveLength= 3e8/Band;
Fig=1;
number=30;
bias=0;
Profile_number=min(10,number);
if Fig==1
    figure(5);hold on;grid on;
    xlabel('Delay (s)');
    ylabel('Path Loss (dB)');
    title('Time Domain');
end
for i=1:number
    fname = ['scen3_pt' num2str(i) '.s1p'];
    fid = fopen(fname, 'rt');
    if fid == -1
    disp(['File cannot be opened !']);
    Hf = 0;  f = 0;
    return;
    end;
        while( 1 )
        temp_str = fgetl(fid);
```

```
    if temp_str(1) == '!'
        if flag_fig == 1
            disp(temp_str);
        end;
    else
        if temp_str(1) == '#'
            tmp_data = fscanf(fid, '%g %g %g', [3 inf] );
            fclose(fid);

            tmp_data = tmp_data.';
            f = tmp_data(:,1);
            amp = 10.^(tmp_data(:,2)/20);
            Hf = amp.*exp(1j*tmp_data(:,3)*pi/180);
            break;
        else
            if feof(fid)
                fclose(fid);
                Hf = 0;   f = 0;
                return;
            end;
        end;
    end;
end;
f_dB=20*log10(abs(amp))-bias;
RSS_dB=mean(f_dB);
RSS=[RSS,RSS_dB];
```

```
    Hf=Hf(P_start:P_stop);
    f=f(P_start:P_stop);
    [zt_han, t] = czt_hanning( f, Hf, tstart, tstop, 1, 1601*10);
    time_dB = 20*log10(abs(zt_han))-bias;
    index = pkd_cir(time_dB, noi, side, peak_width);
    if index == 0
     continue
    end
    ftoa_delay = [ftoa_delay t(index(1))];
    ftoa_amp = [ftoa_amp 20*log10(abs(zt_han(index(1))))-bias];
    if Fig==1 && Profile_number~=0
        figure(5);hold on;grid on;
        plot(t,time_dB,'b');
        figure(5);hold on;
        plot(t(index(1:length(index))),20*log10(abs(zt_
han(index(1:length(index)))))-bias,'bo');
        plot(ftoa_delay,ftoa_amp,'ro');
        Profile_number=Profile_number-1;
    end
        for k=1:length(index)
        PKgain(i,k)= abs(zt_han(index(k)));
        PKdis(i,k)=t(index(k));
        PK(i,2*(k-1)+2) = 20*log10(abs(zt_han(index(k))))-bias;
        PK(i,2*(k-1)+1)=t(index(k))*2.99792458*10^8;
        end
 maxPKgain(i)=max(PKgain(i,1:k));
```

```
end
for i=1:number
    denominator(i) = sum(PKgain(i,:).^2);
    numerator_II(i) = sum((PKgain(i,:).^2).*PKdis(i,:));
    numerator_I(i) = sum((PKgain(i,:).^2).*(PKdis(i,:).^2));
    factor_I(i) = numerator_I(i)/denominator(i);
    factor_II(i) = numerator_II(i)/denominator(i);
    factor_II(i) = factor_II(i)^2;
    rms(i) = sqrt(abs(factor_I(i)-factor_II(i))).*1e9;
end
ftoa_dist=ftoa_delay*2.99792458*10^8;
m=1:1:length(ftoa_dist);
figure(3); hold on; grid on;
title('TOA distance in sequence');
xlabel('Sequence');
ylabel('TOA distance(m)');
plot(m,ftoa_dist,'*-');
```

Bibliography

[AFe05] J. Ryckaert A. Fort, C. Desset and al. et. Characterization of the ultra wideband body area propagation channel. *2005 IEEE International Conference on Ultra-Wideband*, 2005.

[AMp03] J.R. Foerster A.F. Molisch and M. pendergrass. Channel models for ultrawideband personal area networks. *IEEE wireless communications magazine*, 10(6), 2003.

[AP06a] B. Alavi and K. Pahlavan. Modeling of the toa based distance measurement error using uwb indoor radio measurements. *IEEE Communication Letters*, 10(4):275–277, April 2006.

[AP06b] B. Alavi and K. Pahlavan. Modeling of the toa based distance measurement error using uwb indoor radio measurements. *IEEE Communication Letters*, 10(4):275–277, April 2006.

[AP06c] B. Alavi and K. Pahlavan. Modeling of the toa based distance measurement error using uwb indoor radio measurements. *IEEE Communication Letters*, 10(4):275–277, April 2006.

[BLe11] I. Moerman B. Latre, B. Braem and al et. A survey on wireless body area networks. *Wireless Networks*, (1):1–18, January 2011.

[CPe10] D.H. Park C.Y. Park, H. Cho and al et. Aoa localization system design and implementation based on zigbee for applying greenhouse. *2010 5th IEEE International Conference on Embedded and Multimedia Computing (EMC)*, August 2010.

[Cra98] M. Craig. On-body measurements and characterization of wireless communication channel fro arm and torso of human. *Electronic Engineering Times*, (1026):58, 1998.

[DCM02] M.Z. Win D. Cassioli and A.F. Molisch. The ultra-wide bandwidth indoor channel: from statistical model to simulations. *IEEE journal on selected areas in communications*, 20, 2002.

[DDe09] U. Ferner D. Dardari, A. Conti and al et. Ranging with ultrawide bandwidth signals in multipath environments. *Proc. Of IEEE, Special Issue on UWB Technology and Emerging Applications*, Februry 2009.

[EAM11] Y. Li E. Andrea, X. Chen and R.G. Micheal. Rss based node localization in the presence of attenuating objects. *2011 IEEE International Conference on Acoustics*, May 2011.

[FAeA11] Y. Ye F. Askarzadeh and et. Al. A new perspective on the impact of diffraction in proximity of micro-metals for indoor geolocation. *22nd IEEE Personal Indoor Mobile Radio Communications (PIMRC)*, 2011.

[FDRe11] J. Nurmi F. Della Rosa, L. Xu and al et. Hand-grip and body-loss impact on rss measurements for localization of mass market devices. *International Conference on Localization and GNSS (ICL-GNSS)*, pages 58–63, 2011.

[Gp08] M. Garardine and V. prithiviraj. Uwb localization techniques for precision automobile parking system. *IEEE 10th International Conference on Electromagnetic Interference and Compatibility (INCEMIC)*, pages 621–626, November 2008.

[HAP97] M. Hassan-Ali and K. Pahlavan. Site specific wideband indoor channel modelling using ray tracing software. *IET Electronics Letters*, 33(23):1983–1984, 1997.

[HP08] M. Heidari and K. Pahlavan. A markov model for dynamic behavior of toa-based ranging in indoor localization. *EURASIP Journal on Advances in Signal Processing*, 2008, 2008.

[JCP12] Y. Ye J. Chen and K. Pahlavan. Uwb characteristics of creeping wave for rf localization around the human body. *Proceedings of the 23nd annual IEEE international symposium on personal, indoor and mobile radio communications (PIMRC)*, September 2012.

[JHe11a] Q. Zhang J. He, Q. Wang and al et. A practical indoor toa ranging error model for localization algorithm. *2011 IEEE 22nd International Symposium on Personal Indoor and Mobile Radio Communications (PIMRC)*, September 2011.

[JHe11b] Qianxiong Zhang Jie He, Qin Wang and al. et. A practical indoor toa ranging error model for localization algorithm. *2011 IEEE 22nd International Symposium on Personal Indoor and Mobile Radio Communications (PIMRC)*, September 2011.

[JHP12a] Y. Geng J. He and K. Pahlavan. Ieee 23nd international symposium on personal, indoor and mobile radio communications (pimrc12). September 2012.

[JHP12b] Y. Geng J. He and K. Pahlavan. Modeling indoor toa ranging error for body mounted sensors. *2012 IEEE 23nd International Symposium on Personal Indoor and Mobile Radio Communications (PIMRC)*, September 2012.

[JHW12] K. Pahlavan J. He, S. Li and Q. Wang. A realtime testbed for performance evaluation of indoor toa location system. *IEEE International Conference on Communications (ICC)*, June 2012.

[KK09] M. Kawasaki and R. Kohno. A toa based positioning technique of medical implanted devices. *Third International Symposium on Medical Information and Communication Technology*, February 2009.

[KP02] J. P. Makela K. Pahlavan, Li Xinrong. Indoor geolocation science and technology. *IEEE Communications Magazine*, 40:112–118, February 2002.

[KPK12a] R. Fu K. Pahlavan, Y. Ye and U. Khan. Accuracy of localization system inside human body using a fast fdtd simulation technique. *Medical Information and Communication Technology (ISMICT)*, 2012.

[KPK12b] R. Fu K. Pahlavan, Y. Ye and U. Khan. Challenges in channel measurement and modeling for rf localization inside the human body. *International Journal of Embedded and Real Time Communication Systems*, 2012.

[KPM02] X. Li K. Pahlavan and J. Makela. Indoor geolocation science and technology. *IEEE Comm Soc. Mag.*, 40(2), February 2002.

[LS02] J. Lee and R. Scholtz. Ranging in a dense multipath environment using an uwb radio link. *IEEE Journal on Selected Areas in Communica- tions*, 20(9), December 2002.

[NA09a] K. Pahlavan N. Alsindi, B. Alavi. Measurement and modeling of ultrawideband toa-based ranging in indoor multipath environments. *IEEE Transactions on Vehicular Technology*, 58:10461058, 2009.

[NA09b] K. Pahlavan N. Alsindi, B. Alavi. Measurement and modeling of ultrawideband toa-based ranging in indoor multipath environments. *IEEE Transactions on Vehicular Technology*, 58(3):1046–1058, 2009.

[NAP09] B. Alavi N. Alsindi and K. Pahlavan. Measurement and modeling of uwb toa-based ranging in indoor environments. *IEEE Trans. Vehic. Tech.*, 58:1046–58, March 2009.

[NMP06] S. Tompkins N. Moayeri, J. Mapar and K. Pahlavan. Special issuse on navigation using signals of opportunity. *IEEE Wireless Magazine*, 18(4), April 2006.

[NPe05] S. Kyperountas N. Patwari, J.N. Ash and al et. Locating the nodes: cooperative localization in wireless sensor networks. *IEEE signal processing magazine*, 22:54–69, 2005.

[PL05] K. Pahlavan and Allen H. Levesque. Wireless information networks - 2nd edition. 2005.

[QWW09] K. Masami Q. Wang and J. Wang. Channel modeling and ber performance for wearable and implant uwb body area links on chest. *IEEE international conference on Ultra-wide-band (ICUWB)*, pages 316–320, September 2009.

[RFP12] N. Yang R. Fu, Y. Ye and K. Pahlavan. Doppler spread analysis of human motions for body area network applications. *Proceedings of the 22nd annual IEEE international symposium on personal, indoor and mobile radio communications (PIMRC)*, 2012.

[RR03] FCC Rules and Regulations. Mics band plan. *Part 95*, January 2003.

[SLP12] R. Fu S. Li, J. He and K. Pahlavan. A hardware platform for performance evaluation of in-body sensors. *6th IEEE International Symposium on Medical Information and Communication Technology (ISMICT)*, March 2012.

[SPK12] K. Pahlavan S. Pranay and U. Khan. Indoor geolocation science and technology. *IEEE Communications Magazine*, March 2012.

[STM11] H. David S. Thuraiappah and H. Mark. Wasp: A system and algorithms for accurate radio localization using low-cost hardware. *IEEE Transactions on Systems, Man, and Cybernetics, Part C: Applications and Reviews*, 2:211–222, 2011.

[tg610] Draft of channel model for body area network. *IEEE*, November 2010.

[Uni09] International Telecommunication Union. industrial, scientific and medical (ism) applications (of radio frequency energy): Operation of equipment or appliances designed to generate and use locally radio frequency energy for industrial, scientific, medical, domestic or similar purposes, excluding applications in the field of telecommunications. October 2009.

[XCe11] D. Jin X. Chen, X. Lu and al. et. Channel modeling of uwb-based wireless body area networks. *2011 IEEE International Conference on Communications*, June 2011.

[zar] Zl70102 application development kit. *http://www.zarlink.com*.

[ZB12] X. Zheng and G. Bao. The performance of simulated annealing algorithms for wi-fi localization using google indoor map. *IEEE 76th Vehicular Technology Conference (VTC)*, September 2012.